Icarus 333 (2019) 323–342

Contents lists available at ScienceDirect

Icarus

journal homepage: www.elsevier.com/locate/icarus

Iron content determines how space weathering flux variations affect lunar soils

James McFadden[a], Ian Garrick-Bethell[a,b,*], Chae K. Sim[b], Sungsoo S. Kim[b], Doug Hemingway[c]

[a] Earth and Planetary Sciences, University of California, Santa Cruz, USA
[b] School of Space Research, Kyung Hee University, Republic of Korea
[c] Carnegie Institution for Science, Washington, DC, USA

A B S T R A C T

Previous work has established that the solar wind and micrometeoroids produce spectral changes on airless silicate bodies. However, the relative importance of these two weathering agents, the timescales over which they operate, and how their effects depend on composition have not yet been well determined. To help address these questions we make use of the fact that solar wind and micrometeoroid fluxes vary with latitude on the Moon. Previous work has shown that this latitudinally varying flux leads to systematic latitudinal variations in the spectral properties of lunar soils. Here we find that the way in which a lunar soil's spectral properties vary with latitude is a function of its iron content, when we consider soils with 14–22 wt% FeO. In particular, a 50% reduction in flux corresponds to a significant increase in reflectance for 14 wt% FeO soils, while the same flux reduction on 21 wt% FeO soils is smaller by a factor of ~5, suggesting that this brightening effect saturates for high FeO soils. We propose that lower iron soils may not approach saturation because grains are destroyed or refreshed before sufficient nano- and micro-phase iron can accumulate on their rims. We compare our results to the spectral variations observed across the Reiner Gamma swirl, which lies on a high-iron surface, and find it has anomalous brightness compared to our predictions. Swirls in Mare Marginis, which lie on a low iron surface, exhibit brightness differences that suggest reductions in solar wind flux between 20 and 40%. Our inferences suffer from the limited latitudinal extent of the maria and the convolution of micrometeoroid flux and solar wind flux changes with latitude. Superior constraints on how space weathering operates throughout the inner solar system would come from in situ measurements of the solar wind flux at lunar swirls.

1. Introduction

Space weathering is the mechanical and chemical alteration of an airless body's soil by solar wind plasma and micrometeoroids. These alterations change the soil's visible to near-infrared reflectance spectra, complicating the interpretation of its mineralogy (Domingue et al., 2014; Hapke, 2001; Pieters and Noble, 2016). Several methods have been developed to quantify these spectral changes. One early technique used 750 and 950-nm bands to construct the spectral parameter OMAT to map surface maturity (Lucey et al., 2000b). These two bands were also combined to determine the amount of iron (FeO) present in a soil (Lucey et al., 2000a; Lucey et al., 1995; Wilcox et al., 2005). Recently, more sophisticated spectral modeling techniques have been developed to estimate iron abundances (Lemelin et al., 2015), and space weathering products (Trang and Lucey, 2019; Trang et al., 2017). A number of these and other methods have been used to argue that soil spectra vary due to differential exposure to solar wind as a function of latitude (Hemingway et al., 2015; Trang and Lucey, 2019; Yokota et al., 2011), or passage through the Earth's magnetotail (Sim et al., 2017; Trang and Lucey, 2019).

Particularly relevant to this work are the latitudinal variations in the spectral parameter β, defined by Hemingway et al. (2015), to isolate the spectral signature of lunar swirls as distinct from other geologic features, such as immature crater rays and ejecta (Fig. 1a). Briefly, β was derived from trends observed in plots of 750-nm-reflectance vs. the ratio of 950 to 750-nm-reflectance, across the range of pixels found inside and outside of swirls. Previous work had shown that normal, non-swirl pixels plotted in this type of plot could be separated according to the pixel's degree of space weathering ("maturity") or iron content (Lucey et al., 2000a; Lucey et al., 2000b; Wilcox et al., 2005). Surprisingly, however, it was found that the brightest swirl pixels were not simply immature in the manner typically predicted for this type of plot, but rather they formed entirely new trends that partially mimicked a decrease in iron (Garrick-Bethell et al., 2011). This new trend was then parameterized by β. The similarity between variations in β at swirls and β across different latitudes, as discovered by Hemingway et al. (2015), simultaneously supported the hypotheses that swirls are partially shielded from the solar wind by the underlying rock magnetization (Hood and Schubert, 1980) and that solar wind plays an important role in causing spectral changes due to space weathering (e.g. Hapke, 2001; Vernazza et al., 2009).

There are at least two unresolved problems with previous studies of

* Corresponding author at: Earth and Planetary Sciences, University of California, Santa Cruz, USA.
E-mail address: igarrick@ucsc.edu (I. Garrick-Bethell).

https://doi.org/10.1016/j.icarus.2019.05.033
Received 29 January 2019; Received in revised form 8 May 2019; Accepted 14 May 2019
Available online 31 May 2019
0019-1035/

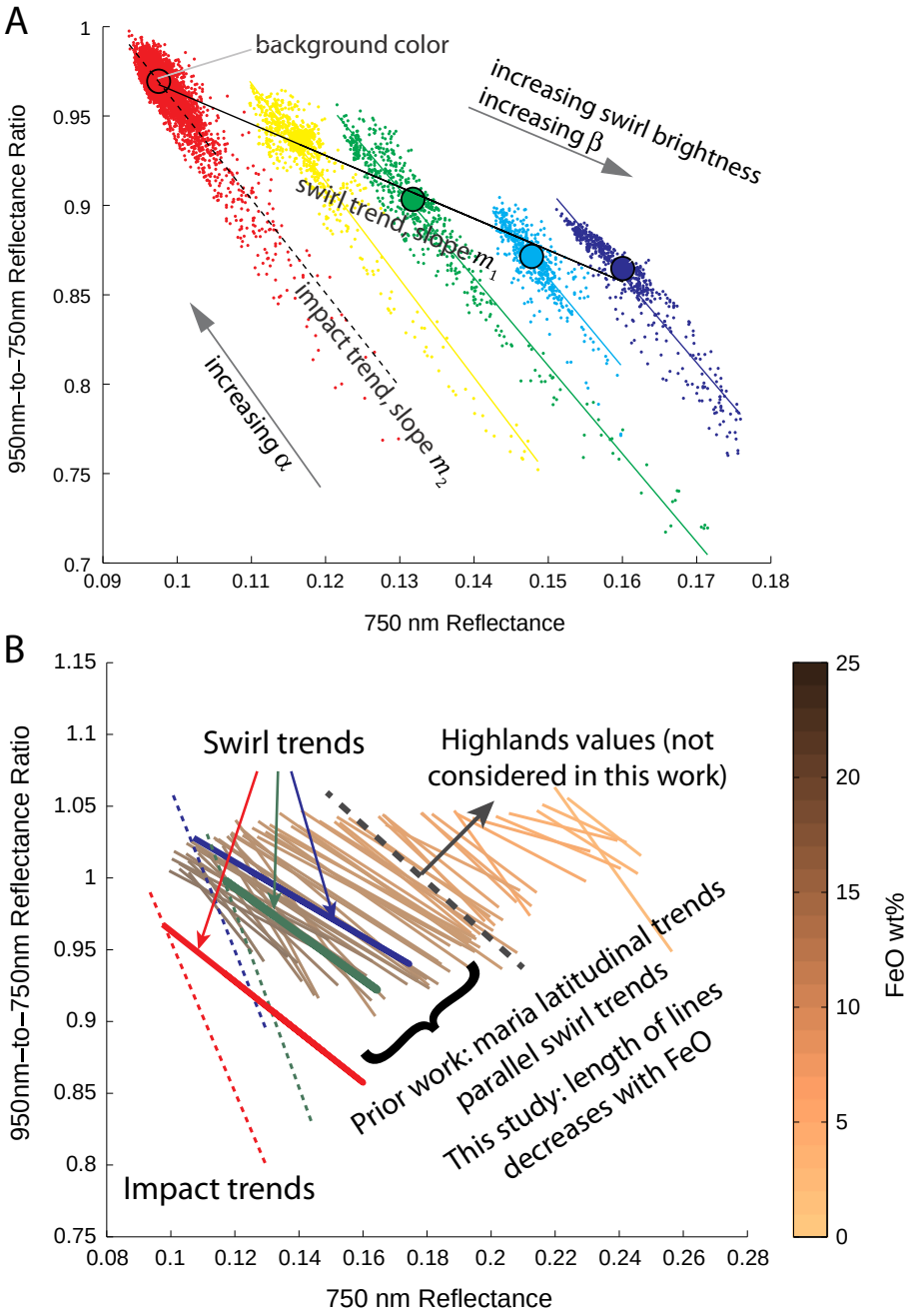

Fig. 1. (A) Definition of the parameter β derived from swirl trends, and distinct from impact trends, observed at Reiner Gamma swirl. (B) Illustration of the similar nature of the spectral change of the lunar maria with latitude, across various iron bins, compared to the spectral changes observed across swirls. Prior work Hemingway et al. (2015) discovered the two trends are parallel. In this work we report the systematic decrease of the length of each line within each iron bin, while the overall shape of the spectral trend is the same across iron bins. Both figures are after those in Hemingway et al. (2015).

the Moon's latitudinal spectral changes. The first is that they do not decouple solar wind and micrometeoroid effects. If micrometeoroids are largely confined to the ecliptic plane, which is the case for larger impactors (Gallant et al., 2009; Le Feuvre and Wieczorek, 2008), their flux should decrease with latitude, just as the solar wind flux. Micrometeoroids likely produce nanophase (< 100 nm) (Loeffler et al., 2008; Sasaki et al., 2002) and microphase (> 100 nm Britt and Pieters, 1994; James et al., 2001; Lucey and Riner, 2011) metallic iron particles that darken and alter a soil's spectrum (collectively referred to herein as submicroscopic iron, following Trang and Lucey, 2019). Solar wind may also be capable of producing submicroscopic iron (Loeffler et al., 2009) (but see Christoffersen et al., 2015), or at least changing the soil spectra via some other mechanism (Fu et al., 2012b; Marchi et al., 2005; Strazzulla et al., 2005). Complicating the matter further, nanophase iron particles may coalesce into microphase iron (Pieters and Noble, 2016), possibly making their abundance partially dependent on both solar wind and micrometeoroids. Remote sensing observations support the importance of micrometeoroids: grain size (Jeong et al., 2015) and microphase iron both decrease with latitude (Trang and Lucey, 2019).

The second unresolved problem is that previous work did not determine how latitudinal spectral variations depend on composition, particularly FeO content. As the regolith is gardened through meteoroid impacts, immature soil grains are introduced into the soil, and mature soil is destroyed or melted (e.g. (Gault et al., 1974)). Thus, the steady state abundance of submicroscopic iron on a surface likely depends on

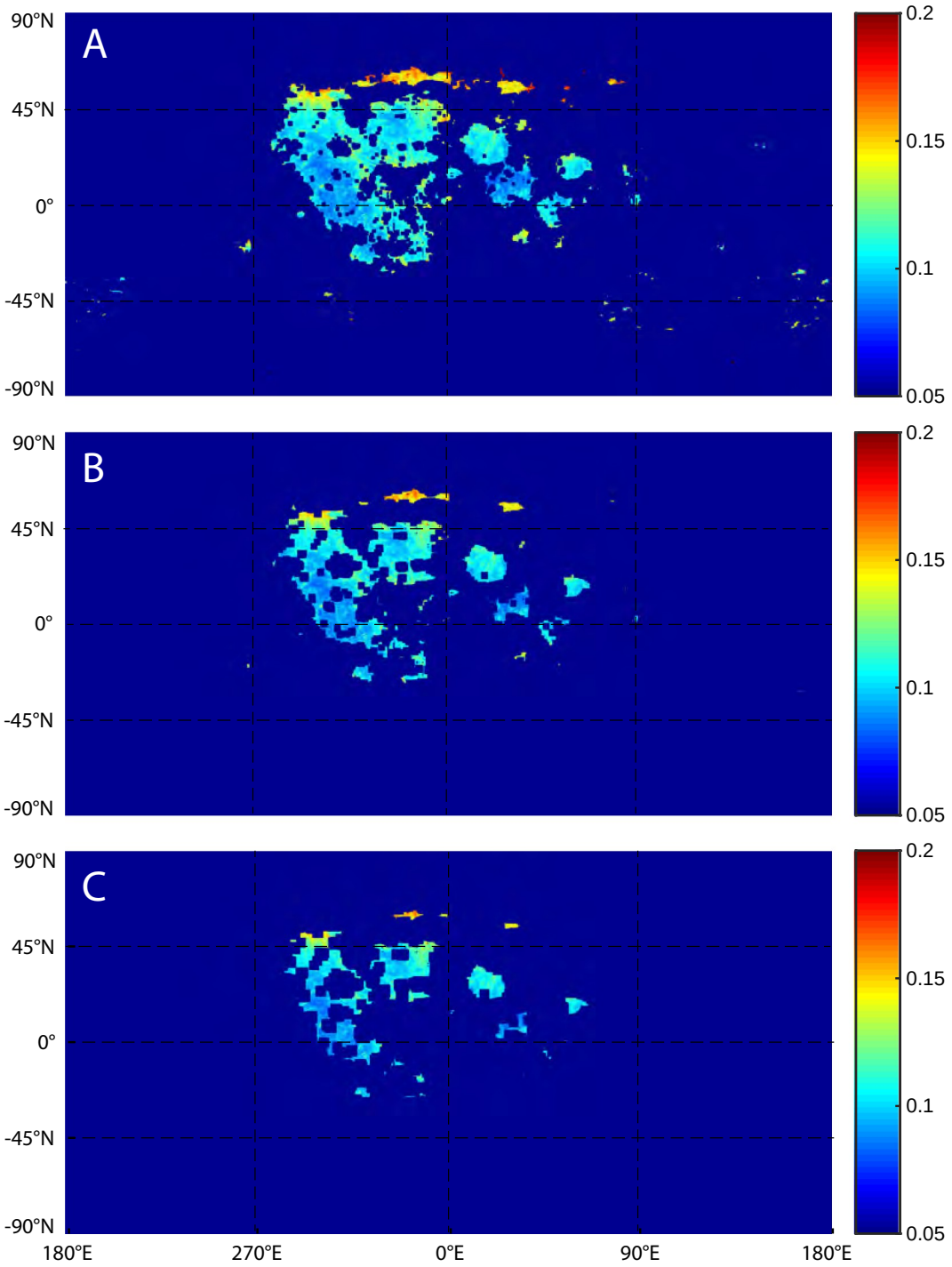

Fig. 2. (A) Clementine 750-nm-reflectance restricted to the maria. (B) Same as panel A, but with a maria-highland boundary standoff distance of 22.5 km. (C) Same as panel A but with a maria-highland boundary standoff distance of 45 km. All maps show the entire Moon in simple cylindrical projection centered on the nearside.

the timescale of the gardening process relative to the timescale for accumulation of submicroscopic iron on rims of exposed grain. Assuming the soil concentration of FeO influences the rate of accumulation, higher iron soils should have higher abundances of submicroscopic iron. Alternatively, one might imagine that soils of all iron content eventually saturate their rims with submicroscopic iron if their accumulation times are much faster than the regolith gardening timescales. Or, perhaps there is a level of FeO above which grains start to exhibit saturation in submicroscopic iron. A possibly related effect was reported in Trang and Lucey (2019), who found that nanophase iron saturates at ~17 wt% FeO, but they did not explain the saturation as function of the flux of weathering agents.

The first objective of this paper is to determine how spectra change as a function of latitude for a given FeO content. The second is to compare those trends with those observed at swirls, where the micrometeoroid flux is likely uninterrupted, to gain some insight into the importance of micrometeoroids in space weathering, possibly as a function of FeO. A hint that the latitudinal variation depends on FeO content can be found in Hemingway et al. (2015). A reproduction of their work in Fig. 1b shows the spectral trends characteristic of swirls and the lunar maria across different latitudes, for soils of various FeO content. The similar slopes of these lines and the lines at swirls imply

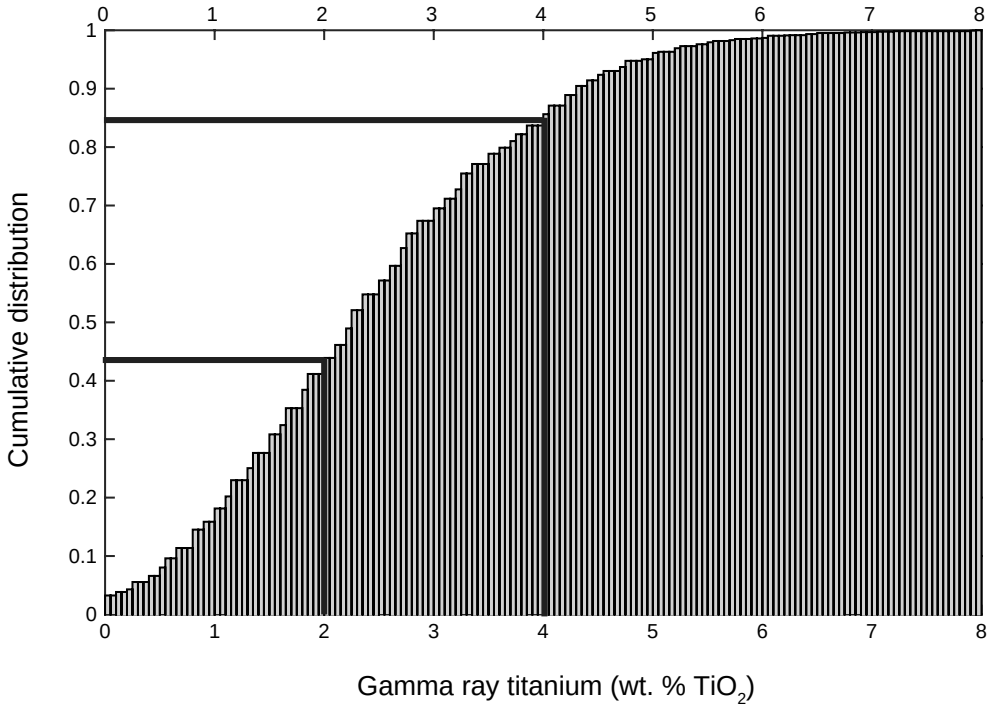

Fig. 3. Cumulative distribution of Lunar Prospector titanium (wt% TiO2), restricted to the lunar maria. The two bins used in our nominal analysis are indicated with black lines (0–2 wt% and 2–4 wt% TiO_2).

that high latitude regions and swirls change their spectra in similar ways due to reduced solar wind flux, as discussed above. However, the length of these lines was not considered in Hemingway et al. (2015). The length of the lines decreases with increasing FeO, implying that even though the spectral trends are the same across surfaces with variable FeO content, the total range of variation in β decreases at higher FeO concentrations. In contrast, lower FeO soils on the maria are more susceptible to spectral changes, as shown by their longer lines (here we are ignoring the lines with very low iron that fall on the highlands, which also exhibit shortening). In the next sections we present a more quantitative characterization of this effect on the lunar maria. We restrict our analysis to the lunar maria because they exhibit the spectral effects of space weathering more strongly, as reported previously (Hemingway et al., 2015; Lemelin et al., 2016). This stronger effect of weathering in the maria is presumably due to the overall higher abundances of FeO, compared to the highlands, and the fact that FeO is putatively the dominant source of submicroscopic iron. Another reason we restrict our coverage to the maria is that the range of iron content is smaller over the highlands, especially when considering our analysis must avoid iron quantitates that are intermediate between highlands and maria (see Methods).

The second objective of this paper is to use the results from the maria to calculate the predicted spectral changes at two lunar swirls found on surfaces with different FeO concentrations. The solar wind flux at swirls is unknown, but we can explore the assumption that the flux is reduced to nearly zero at the swirl associated with some of the strongest magnetic fields on the Moon: Reiner Gamma.

2. Methods

To determine how iron influences the spectral response at high latitudes, we use a map identifying the lunar maria based on topographic roughness, as in previous work (Hemingway et al., 2015; Kreslavsky et al., 2013). Using topographic roughness to define the maria-highlands boundary avoids defining it with spectral data, which may vary with latitude. We use Lunar Prospector (LP) gamma-ray spectrometer (GRS) iron (wt% FeO) at a resolution of 2 pixels per degree (ppd) (Lawrence et al., 2002), to characterize the surface FeO content. As discussed in Hemingway et al. (2015), GRS iron abundances are not affected by space weathering or interpretations of lunar spectra. Other global-scale spectrally derived maps of FeO are available (Lemelin et al., 2015), and we note there may be differences between their FeO estimates and those obtained from LP.

We then combine GRS iron with three different measures of spectral variation. The first is Clementine 750 nm reflectance (R_{750}), the second is Lunar Orbiter Laser Altimeter (LOLA) reflectance at 1064 nm (R_{LOLA}) (Lucey et al., 2014), and the third is the spectral parameter β, discussed above. We used R_{750} and β datasets sampled at 16 ppd. The resolution of the LOLA data is 4 ppd. We also bin our data according to LP GRS titanium (wt% TiO_2) (Prettyman et al., 2006) with a map resolution of 0.5 ppd. We avoid spectrally derived estimates of titanium (e.g. Sato et al., 2017), due to possible interference with the spectral effects we are measuring.

We also use R_{750} from the Kaguya Multiband Imager (MI) (Ohtake et al., 2008) and the parameter β derived from Kaguya 750-nm and 950-nm-reflectance, to assess whether there are any differences compared to Clementine data. Unlike Clementine data, the Kaguya data we use are corrected for topographic slope. We used data sampled at a resolution of 16 pixels per degree (ppd). The derivation of β using Kaguya data from three lunar swirls is given in Appendix A.

As in Hemingway et al. (2015), we limited our analysis to maria pixels that are sufficiently distant from the maria-highland boundary. Lunar Prospector GRS iron data have a spatial footprint of ~45 km^2 (Lawrence et al., 2002), and therefore the iron values of the maria measured close to a highland boundary will consist of a mixture of iron from the highlands and maria. In this study, we restrict our analysis of the maria to four standoff distances from the nearest highlands boundary: 22.5, 45, 67.5, and 90 km (Fig. 2). Hemingway et al. (2015) showed that using data 50 km from the maria-highland boundary produced no change in the spectral trends we observed. Here we show that the results at half the GRS iron footprint length scale (22.5 km) are nearly identical to those at 45 km, and these estimates form the basis of

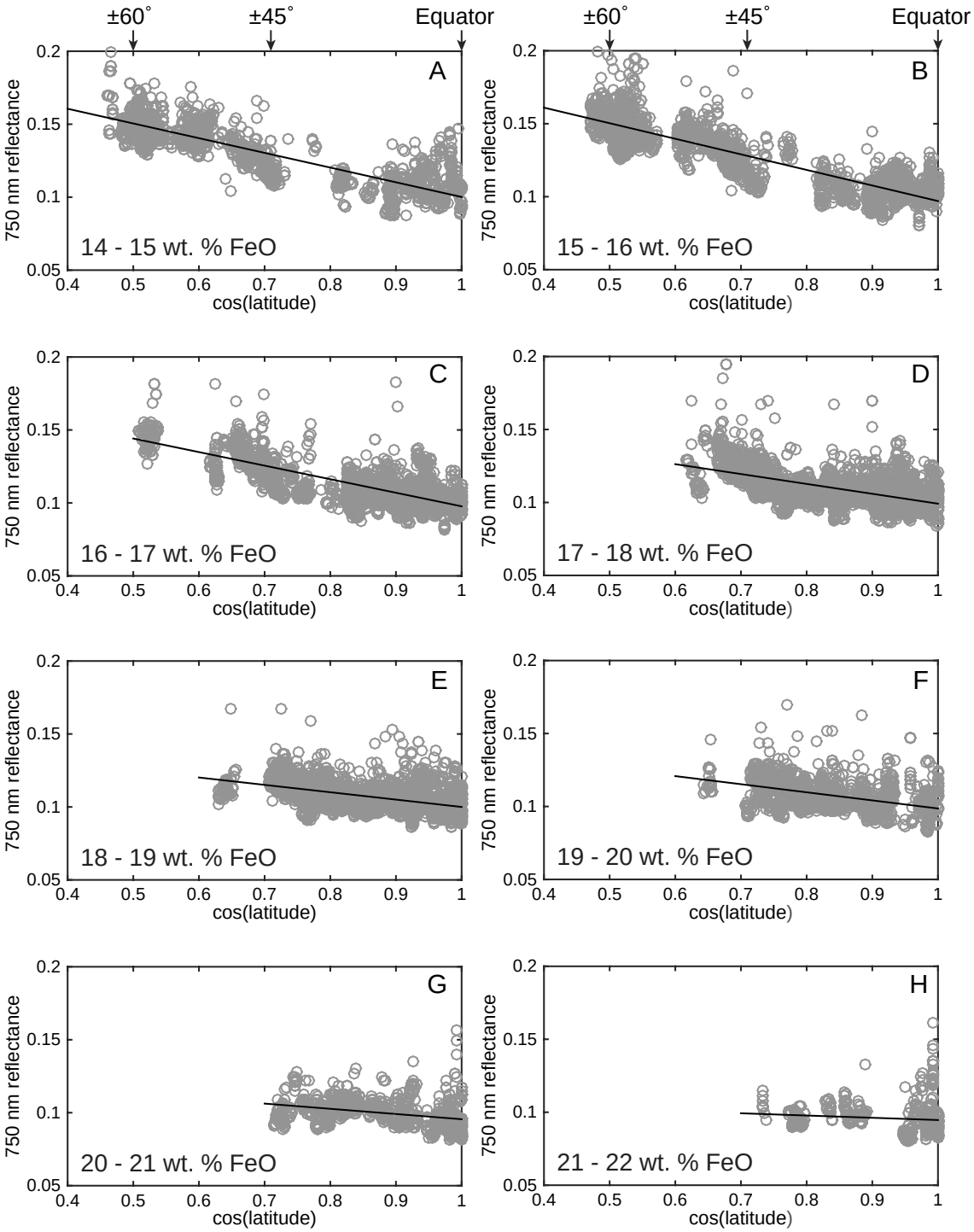

Fig. 4. 750-nm-reflectance vs. cos(latitude) for eight iron bins on the lunar maria, for 0–2 wt% TiO_2 and reflectance pixels restricted to a standoff distance of 22.5 km from the maria-highland boundary. Black lines show the best-fit line. Fig. 5 shows the best-fit line slopes for each iron bin.

our conclusions. The standoff distances of 67.5 and 90 km are extreme values explored to test the robustness of the effects we observe. In practice, to remove maria pixels within a given distance from the highland boundary, we progressively remove adjacent pixels until the desired distance is achieved.

We divided GRS iron into bins of 1 wt% FeO and then further subdivided our analysis by GRS titanium, as in Hemingway et al. (2015). We use two TiO_2 bins in our nominal analysis: 0–2 and 2–4 wt%. Fig. 3 shows the distribution of TiO_2 restricted to the maria, illustrating that ~85% of the lunar maria are covered by TiO_2 values up to 4 wt% (later, we also consider the full range of TiO_2 up to 8 wt% to determine if our results are artifacts of lower data availability at high latitudes). An example of how R_{750} changes with latitude, for eight iron bins, for 0–2 wt% TiO_2 is shown in Fig. 4. As in Hemingway et al. (2015), we use cos(latitude), instead of simply latitude, since the cosine function provides a linear decay of solar wind and (approximately) micrometeoroid flux with latitude. We exclude maria pixels with FeO < 14 wt% since we were concerned that such pixels may harbor a component of highlands contamination. We excluded iron content > 22 wt% FeO since the number of pixels available above this iron bin is limited to near-

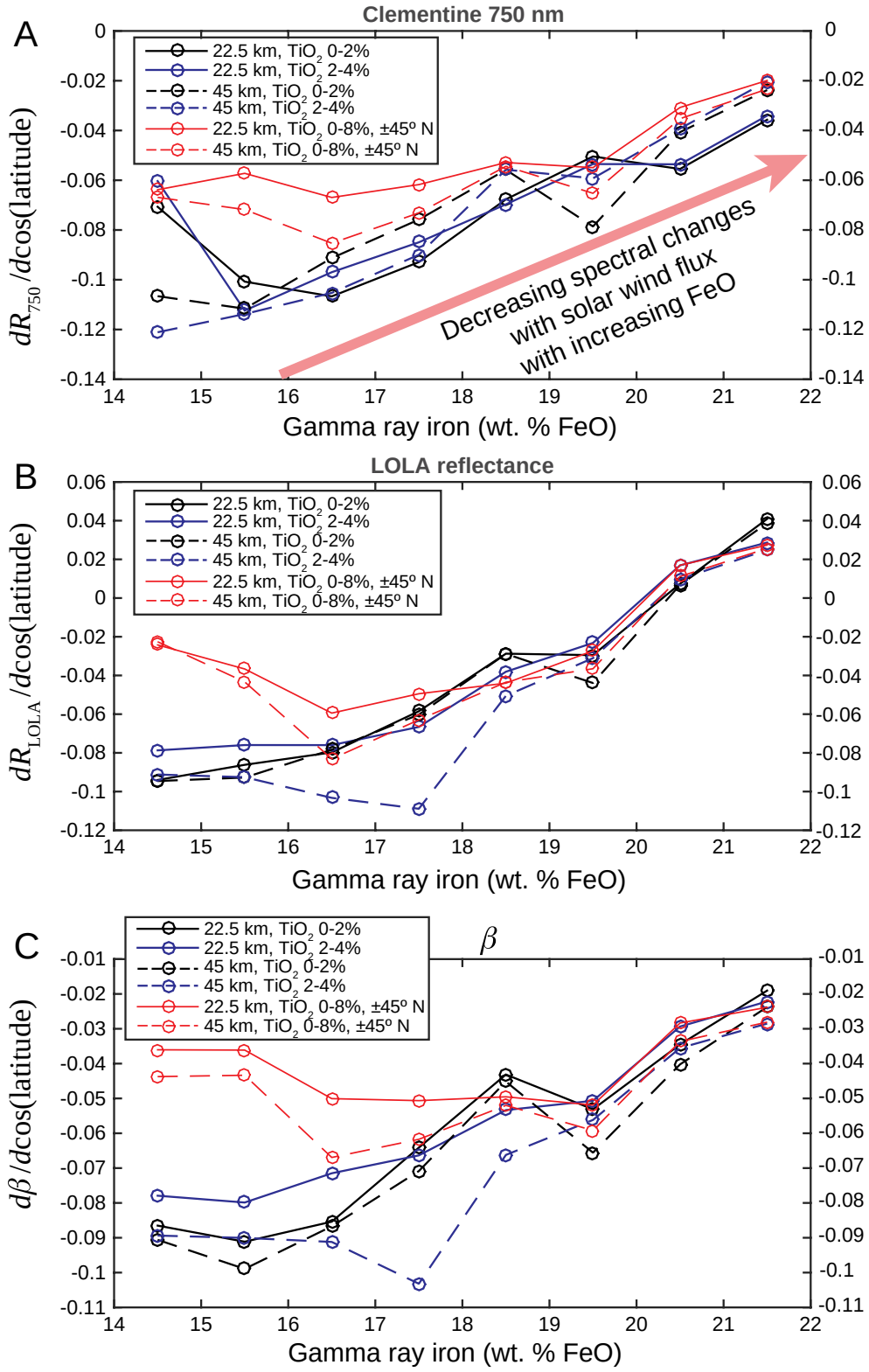

Fig. 5. (A) Rate of change of Clementine 750-nm-refletance with cos(latitude), $dR_{750}/d\cos(\text{latitude})$, for eight iron bins on the lunar maria, three titanium bins, and maria-highland standoff distances of 22.5 and 45 km (see legend). Red lines show data restricted to ± 45° of the equator (and 0–8 wt% TiO_2, see Fig. 8). (B) Same as panel A but for LOLA reflectance. (C) Same as panel A but for the spectral parameter β (Clementine derived). All data points are at the center of each iron bin, i.e. every half integer. (For interpretation of the references to colour in this figure legend, the reader is referred to the web version of this article.)

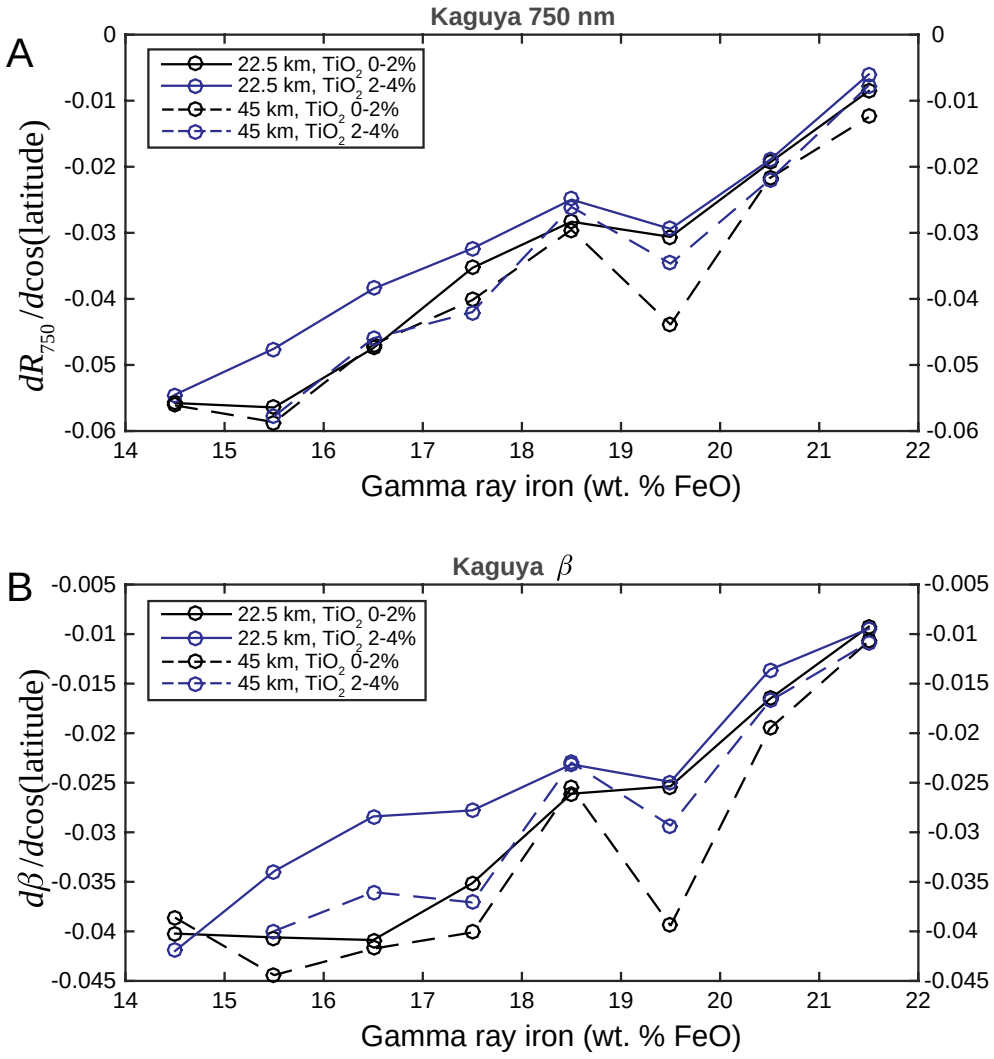

Fig. 6. (A) Same as Fig. 5a, but for Kaguya 750-nm-reflectance. (B) Same as for Fig. 5b, but for the spectral parameter β derived from Kaguya data.

equatorial regions. The minimum latitudinal extent of any of the eight iron bins used was ± 45° from the equator, which was present in the 21–22 wt% iron bin. We calculated the best-fit slopes for each of the cos (latitude) plots such as those in Fig. 4, via a simple least squares line fit. We then repeated the analysis for the 2–4 wt% TiO_2 bin, and then again for a maria-highland standoff of 45 km.

3. Results: maria trends

Overall, we find that R_{750} increases with decreasing cos(latitude) (i.e. R_{750} increases poleward), as expected. Moreover, for high iron bins, this rate of increase, dR_{750}/dcos(latitude) (i.e. the slope of the best-fit line, see Fig. 4), slows dramatically (i.e. its negatively valued slope approaches zero, Fig. 5a). Similar trends are observed for R_{LOLA} (Fig. 5b), and β (Fig. 5c). Later, we show that this effect is not due simply to higher FeO materials being generally darker in their pristine state (Section 4.1). Similar trends are also observed for Kaguya R_{750} and β (Fig. 6), illustrating that this effect is not an artifact of the dataset used. For Kaguya data, the trend in β is more robust (i.e. the slope is more uniformly increasing), perhaps due to the different topographic calibration of these data.

Interestingly, in the case of R_{LOLA}, the rate of change dR_{LOLA}/dcos (latitude) becomes positive for > 20 wt% FeO (Fig. 5b). This would imply the maria actually darken at high latitudes for high FeO concentrations. However, the apparent positive valued slope may be an artifact of the lower resolution of the LOLA data compared to the Clementine data (4 ppd. vs. 16 ppd). We attempted to resolve this problem by improving our statistics: we performed the dR_{750}/dcos(latitude) vs. FeO analysis in one large titanium bin of 0–8 wt% TiO_2, but the positive valued slopes persisted and were nearly identical. Furthermore, we expanded our analysis to one additional higher FeO bin (22–23 wt% FeO), which was afforded to us by the larger number of pixels when aggregating all titanium bins. However, the slope increased to +0.035, suggesting a monotonic increase of the slope above zero from ~20 wt% FeO. Hence, we have no completely satisfactory explanation for this effect. If the effect is real (i.e. not an artifact of statistics), it may be due to the unique geometry of the LOLA observation at zero phase angle, somehow coupled to the FeO content of the soil. This remains a puzzle for future study.

Note that formal confidence limits on the slopes in Fig. 5 are small due to the large number of points, and so they are not shown. Instead, the uncertainty on the slope is dominated by data coverage, crater rays,

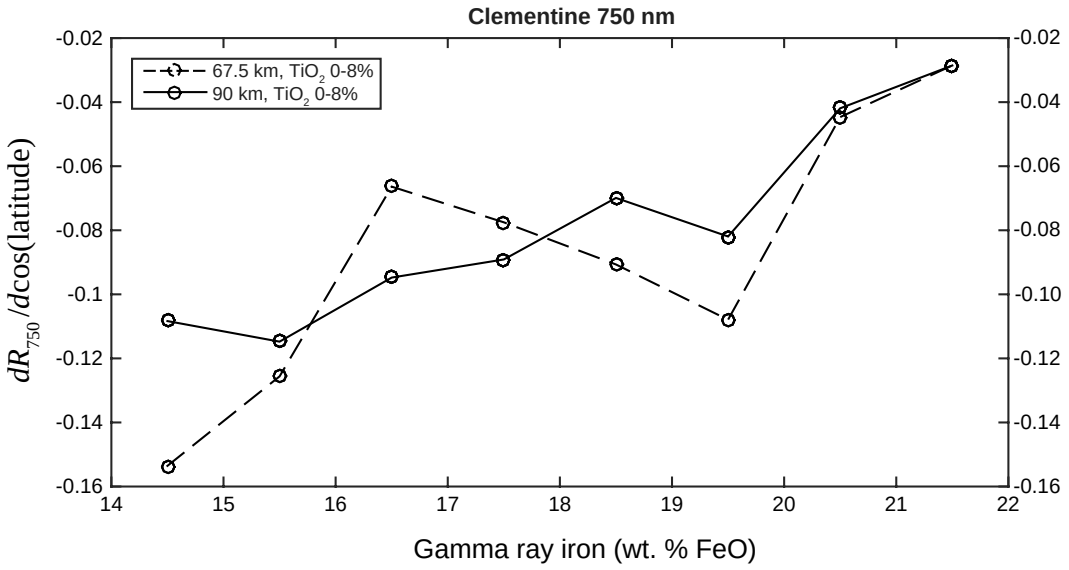

Fig. 7. Same as Fig. 5a, but for maria-highland boundary standoff distances of 67.5 and 90 km, for all titanium data (0–8 wt% TiO_2). Note the different y-axes between this figure and Fig. 5a.

imperfectly removed highland pixels, etc. A number of such potential problems were addressed by Hemingway et al. (2015) and shown not to influence the global-scale trends they observed, suggesting they do not play a role in our observations. But again, we do not exclude their role in some local deviations, including a positive valued $dR_{LOLA}/d\cos(\text{latitude})$ in Fig. 5b.

We also used a more extreme maria-highland standoff distance to determine whether the latitudinal trend could be an artifact of highlands contamination of the GRS FeO abundances near maria-highlands boundaries. We performed our analysis excluding maria pixels within 67.5 and 90 km of the maria-highlands boundary, but we included all titanium data (0–8 wt%), due to the smaller number of pixels available with such a large standoff distance. Using one large titanium bin is justified by the observation that titanium did not affect the results when they were binned by 0–2 and 2–4 wt% TiO_2 (Figs. 5 and 6). Overall, we found that the trend of $dR_{750}/d\cos(\text{latitude})$ increasing with high iron persisted (Fig. 7).

In our analysis we were also concerned that the limited latitudinal range of data in the higher iron bins (e.g. $< 45^\circ$ for 21–22 wt% FeO, see Fig. 4h) could be distorting our results. For example, it might be that the true R_{750} vs. cos(latitude) trend is more like a polynomial or some other function that starts out nearly flat near the equator, and increases more rapidly with increasing latitude, such that a line fit close to the equatorial region yields lower slopes than a line fit to a larger latitudinal range. Or, the true trend may indeed be linear, but simply poorly fit due to the lower latitudinal range of pixels at high iron bins. Therefore, we repeated the same analysis for all eight iron bins, but limiting ourselves to data up to $\pm 45^\circ$ of the equator – the same range as the iron bin with the smallest latitudinal range (21–22 wt% FeO, Fig. 4h). In this case, we had fewer pixels to work with, and we therefore again extended our analysis to include all titanium bins (0–8 wt% TiO_2). We found the trend of $dR_{750}/d\cos(\text{latitude})$ increasing with high iron persisted even when the fit was restricted to data $\pm 45^\circ$, albeit with some greater fluctuations (red lines in Fig. 5 and data in Fig. 8). Note that by limiting our analysis to $\pm 45^\circ$ of the equator we excluded the high-latitude Mare Frigoris.

In summary, we conclude the increase of $dR_{750}/d\cos(\text{latitude})$ with iron is not an artifact of the lower latitudinal coverage of the higher iron bins. The increase is also not limited to a certain range of TiO_2 values. In the remainder of our work we rely on the more robust analysis of data from all maria latitudes (black and blue lines in Fig. 5).

4. Discussion

4.1. Predicted maria 750-nm-reflectance at the equator and $\pm$ 60° N

We next compared the observed R_{750} at low latitudes with the predicted R_{750} at high latitudes. Note that this predicted value included latitudes above the range of actual observations, for some higher iron bins. The low latitude R_{750} was computed from the mean R_{750} value from pixels within $\pm 5^\circ$ of the equator (Fig. 9a). In this case, we had ample pixels to work with up to an iron bin of 23–24 wt%. We also compared these means to the predicted values at the equator from the best-fit lines (Fig. 9b). We found good agreement between the predicted equatorial value and the empirical equatorial mean values (compare Fig. 9a and b), as expected.

Surprisingly, we found that there was only a minor difference of < 0.01 in the equatorial reflectance across all iron bins between 14 and 24 wt% FeO. That is, the darkest state that any soil can reach on the lunar maria (i.e. at the equator), due to solar wind and micrometeoroid effects, is apparently nearly independent of its iron content.

When we calculate the predicted R_{750} value of the soil at higher latitudes, based on the best-fit slopes and y-intercepts from the analysis above (Fig. 5), we find that the predicted R_{750} steadily increases for lower iron bins, as expected. In particular, we computed the predicted R_{750} value at 60° N, which represents a 50% reduction in weathering flux compared to the equator (Fig. 9). We found that the highest iron bin (21–22 wt% FeO) only brightens by about 0.01 at 60° N, while the lowest iron bin (14–15 wt% FeO) brightens by about 0.05. That is, the highest iron soils do not appreciably brighten at high latitudes, compared to their low iron counterparts.

Note that one might also attempt to predict the R_{750} value at higher latitudes from merely the slopes shown in Figs. 5 and 6, and the mean values at the equator (Fig. 9a). However, this ignores the importance of the best-fit y-intercepts in predicting the actual spectral properties at a given latitude.

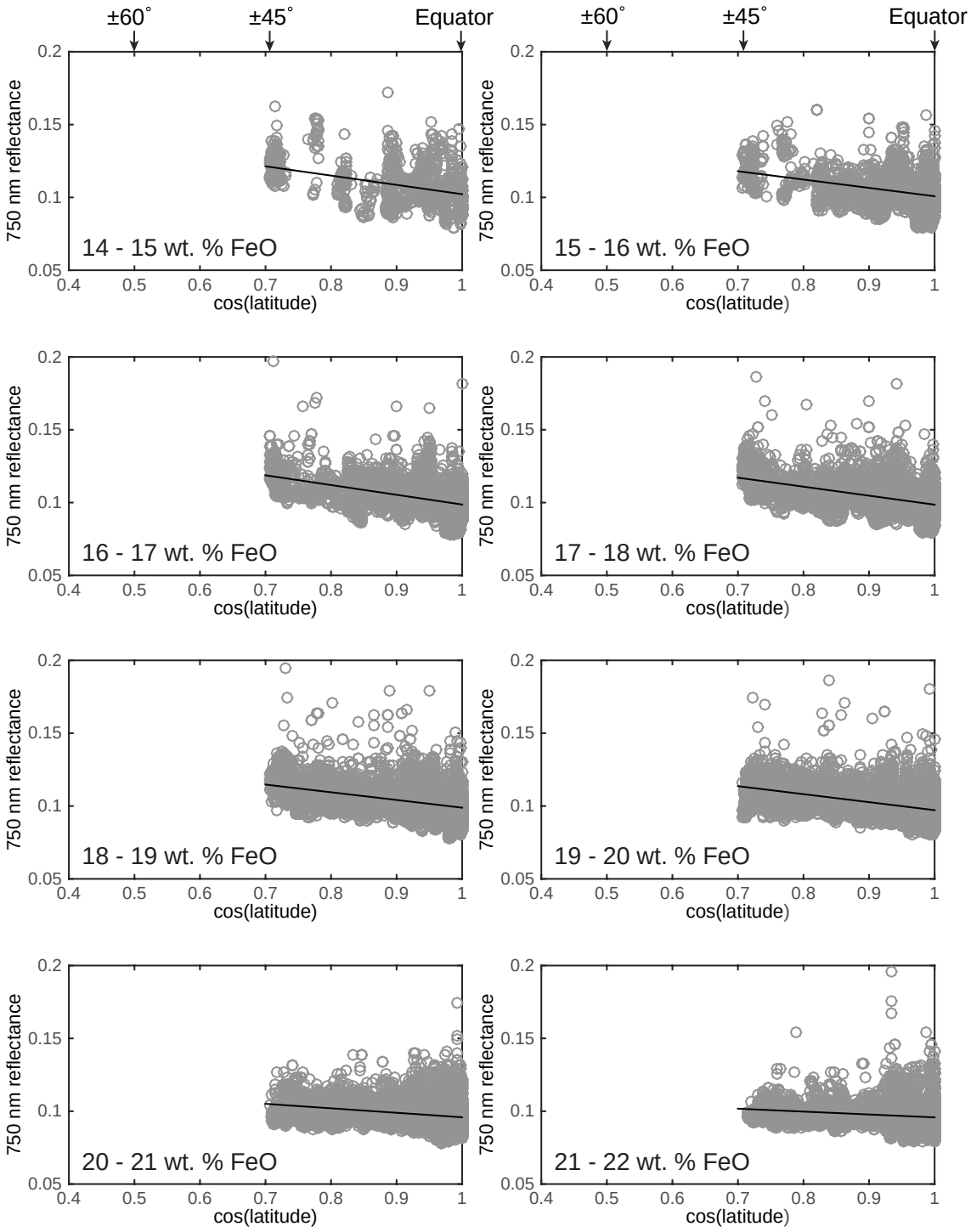

Fig. 8. Same as Fig. 4, but the data and fit are limited to data falling between ± 45˚ of the equator, and all titanium bins are included (0 to 8% wt% TiO_2). Fig. 5 shows the best-fit line slopes for each iron bin (red lines in that figure). (For interpretation of the references to colour in this figure legend, the reader is referred to the web version of this article.)

4.2. Comparisons with spectral variations at swirls

An important question is whether the differences in R_{750} at 60˚ N in Fig. 9 across different iron bins are simply due to higher iron soils being darker than lower iron soils, and their pristine unweathered state is reached at higher latitudes. To answer this question, we compare our predicted spectral values at 60˚ N with observations at swirls on high and low iron mare surfaces. We do not know the solar wind flux reduction at swirls, but they are likely arresting at least protons to some degree. Reiner Gamma is fortuitously near the equator (7˚ N), simplifying our analysis. Reiner Gama is found on a surface with approximately 21 wt% FeO (Fig. 10). The R_{750} at Reiner Gamma varies from a background (non-swirl) value of ~0.095 to a peak near 0.15. These values are taken from pixels outside of fresh craters, within the bright regions shown in Fig. 11 (black boxes). The peak R_{750} at Reiner Gamma (shown in Fig. 9) is substantially brighter than the equatorial value for this iron bin, and nearly equals the predicted R_{750} values for lower iron bins at 60˚ N. Therefore, we conclude that the trends we observe are not

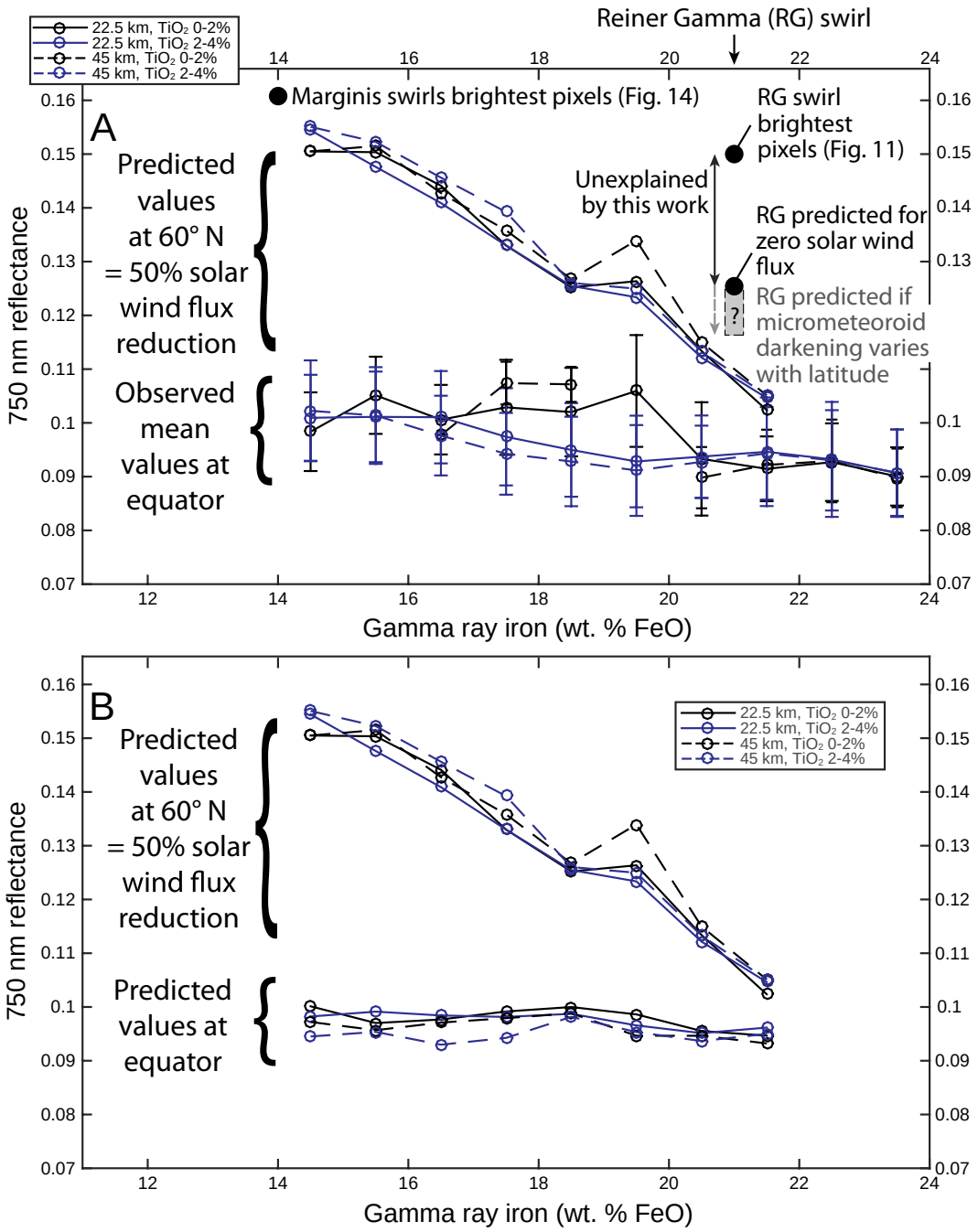

Fig. 9. (A) Bottom curves: Mean Clementine R_{750} values (± 1σ) for pixels within ± 5° of the equator, for eight iron bins, two titanium bins, and maria-highland boundary standoff distances of 22.5 and 45 km. There are no data at 19.5 wt% FeO for the 0–2 wt% TiO_2 bin with a standoff distance of 45 km. Top curves: R_{750} values predicted at 60° N using the best fit linear relationships between R_{750} and cos(latitude) (best-fit slopes shown in Fig. 5). Also shown are the FeO and brightest empirically observed R_{750} values from the swirls considered in Section 4.3 (black dots, see Figs. 11 and 14). The gray range below the predicted Reiner Gamma reflectance shows the expected additional darkening from micrometeoroid weathering, if the latitudinal trends are a combination of both solar wind and micrometeoroid reduction with latitude. (B) Same as in part A except the bottom curves are the 750-nm-reflectance value at the equator obtained from the best-fit linear relationship between R_{750} and cos(latitude). All data points are at the center of each iron bin, i.e. every half integer.

merely due to higher iron soils having generally darker reflectances in the absence of weathering.

We can now perform a more detailed comparison between our predictions of the $dR_{750}/d\cos(\text{latitude})$ trend and the reflectance variations at swirls. Above we concluded that the highest and lowest iron bins only brighten by about 0.01 and 0.05, respectively, when the weathering flux is reduced by 50% (i.e. at 60° N, Fig. 9). We assume that both solar wind flux and micrometeoroid flux control the soil spectral response. We further assume that the spectral variations with latitude embody both a solar wind and micrometeoroid component. If the solar wind flux at Reiner Gamma is zero, we predict R_{750} to be reduced by at least ~0.03. This value is simply (and somewhat crudely) obtained from twice the R_{750} difference between the equatorial pixels and 60° N (=50% flux reduction) for FeO = 21 wt% (see Fig. 9a).

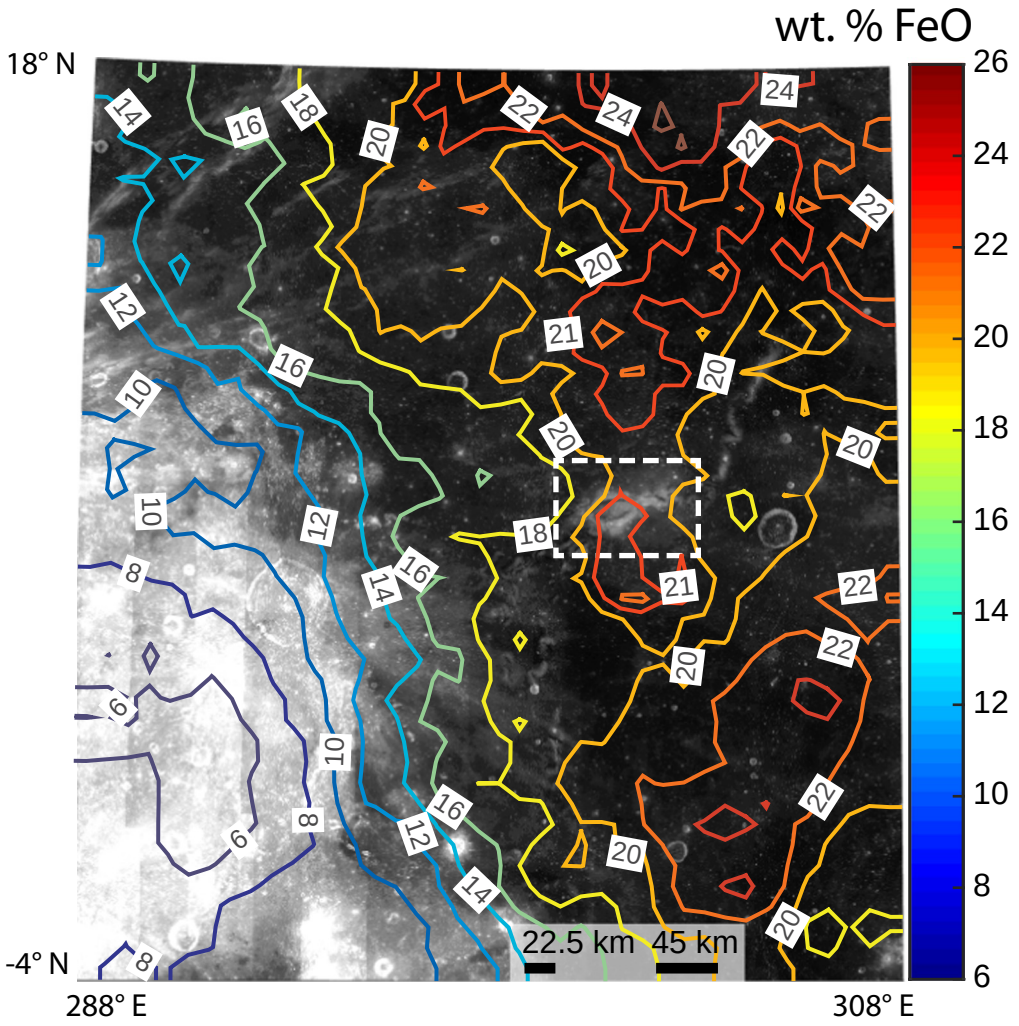

Fig. 10. Lunar Prospector iron (wt% FeO) contours over Clementine 750 nm reflectance in the vicinity of Reiner Gamma swirl (white dashed box). Stereographic projection centered at (7° N, 301° E).

Above we found a total R_{750} change of ~0.055 by examining the actual reflectance values at Reiner Gamma. Therefore, Reiner Gamma appears to be anomalously bright at 750 nm by at least ~80%, relative to our model, or more, if its solar wind flux is not reduced to zero. In Fig. 9a we show the possible further expected reduction of brightness due to micrometeoroids as a gray box under our predicted values from the best-fit function to the latitudinal FeO trend (the vertical extent of this box is speculative). That is, we would have predicted the brightness at Reiner Gamma to have increased by < 0.03, if our $dR_{750}/d\cos(\text{latitude})$ trend is comprised of micrometeoroid and solar wind effects, since the micrometeoroid flux at Reiner Gamma is likely unimpeded (and thereby presumably causing darkening).

We offer two possible explanations that could help reduce the excess model-derived component of brightness at Reiner Gamma: 1) The true R_{750} vs. cos(latitude) function brightens non-linearly as the weathering flux is reduced below the range we have fit. We have only performed our analysis over the region from the equator to a maximum of ~65° N representing a ~58% flux reduction (Fig. 4). However, when the flux gets close to zero at higher latitudes, the R_{750} function may deviate from linearity, and the brightness may increase markedly. Other work has reported non-linear reflectance changes as a function of exposure to space weathering agents (Kohout et al., 2014; Nesvorný et al., 2005; Vernazza et al., 2009). 2) Our analysis is sufficiently in error even though the true R_{750} vs. cos(latitude) function is nearly linear, and we are not able to accurately predict the flux within ~0.025, which is the deviation of Reiner Gamma from predictions in the case of complete solar wind shielding. Since we do not know the actual solar wind flux reduction at Reiner Gamma, and we do not know the actual contribution of micrometeoroids to weathering, it is not possible to conclusively rule in favor of either of these explanations, and the high reflectance at Reiner Gamma remains a puzzle.

Interestingly, Reiner Gamma's top 10% brightest pixels, equal to $R_{750} > 0.14$, represent the top 5% brightest pixels on the entire lunar maria (Fig. 12). Recall that Reiner Gamma falls on a high iron surface near the equator, and such surfaces are typically the darkest on the maria (Fig. 9a). The fact that Reiner Gamma's brightest pixels are the brightest on the maria further illustrates the peculiarity of its ≳80% excess brightness.

Finally, we can compare our predictions with observations of reflectances at swirls on a mare surface with low iron content: Mare Marginis. Much of Mare Marginis and its swirls are close to highland boundaries, making their GRS iron abundances indeterminate.

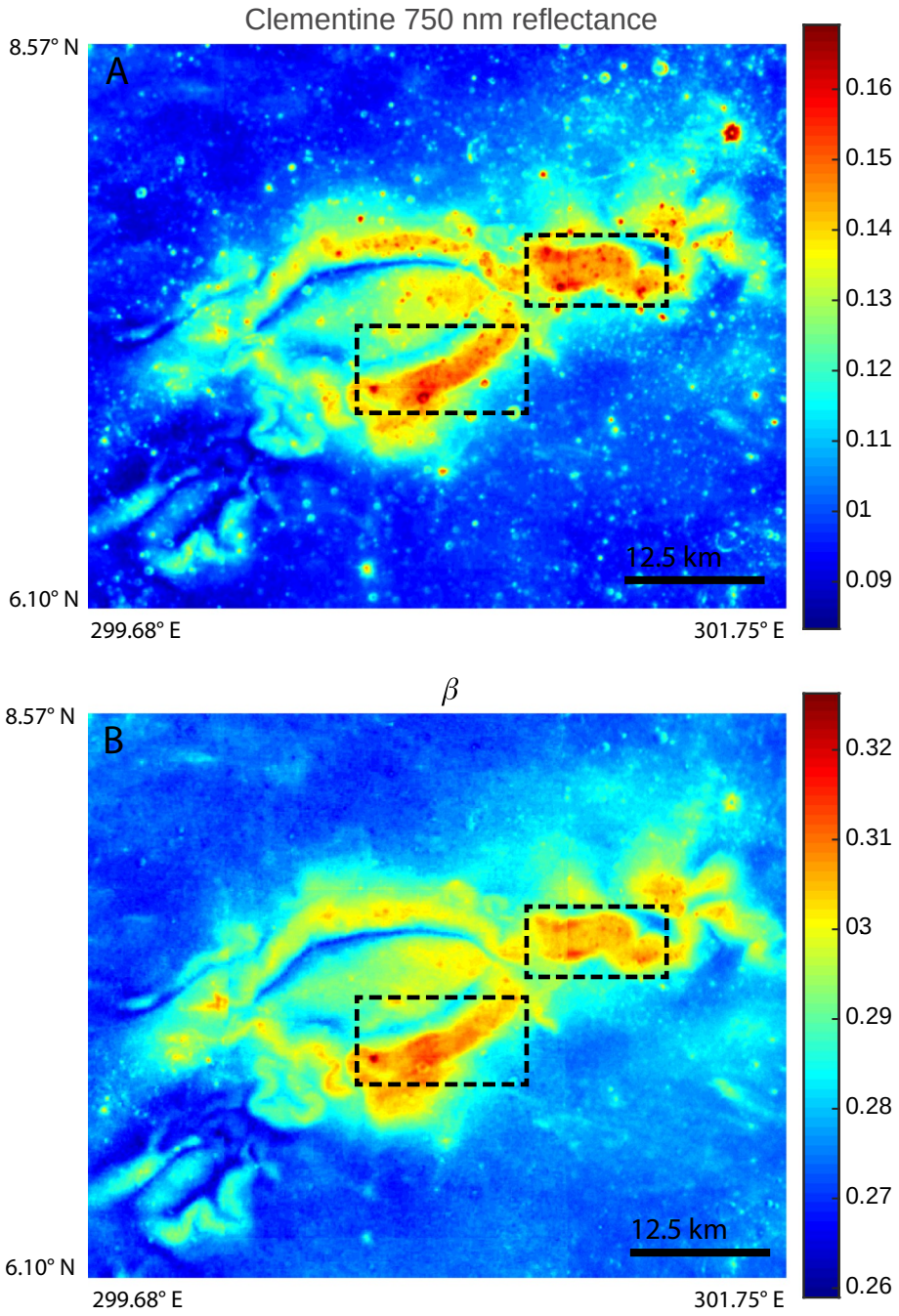

Fig. 11. (A) Clementine 750-nm-reflectance at Reiner Gamma. (B) Spectral parameter β (Clementine derived) at Reiner Gamma. Black dashed boxes illustrate the brightest portions of Reiner Gamma and are discussed in the text. Both maps are cylindrical projection.

However, in central Mare Marginis we find a peak iron concentration of 14% FeO (Fig. 13). We assume this value is representative of the mare values elsewhere in the region. This iron abundance represents the lowest iron bins we examined (Fig. 9). Two well-defined swirls in northwest Mare Marginis have R_{750} of ~0.135 and ~0.155 (black boxes L and H, respectively, in Fig. 14). The peak brightness outside of fresh craters is ~0.16, shown in Fig. 9. The background (non-swirl) reflectance is approximately 0.115, making the total increase in R_{750} ~0.02 and ~0.04, respectively. Again, assume the solar wind and micrometeoroids both vary with latitude. From Fig. 9 we see that the predicted R_{750} change here is ~0.05 for a flux reduction of 50% (using the 14–15 wt% FeO bin). Extrapolating linearly, we would conclude these swirls are shielded by at least ~20% and 40%, respectively (the value may be larger if they are darkened by micrometeoroids). Unlike Reiner Gamma, there is no excess brightness. However, as with Reiner Gamma, we do not know the actual solar wind flux reduction at these regions, or the contribution from micrometeoroids.

4.3. Implications for weathering mechanisms

Our results suggest that the highest iron (> 21 wt% FeO) soils are nearly saturated by submicroscopic iron across the weathering fluxes

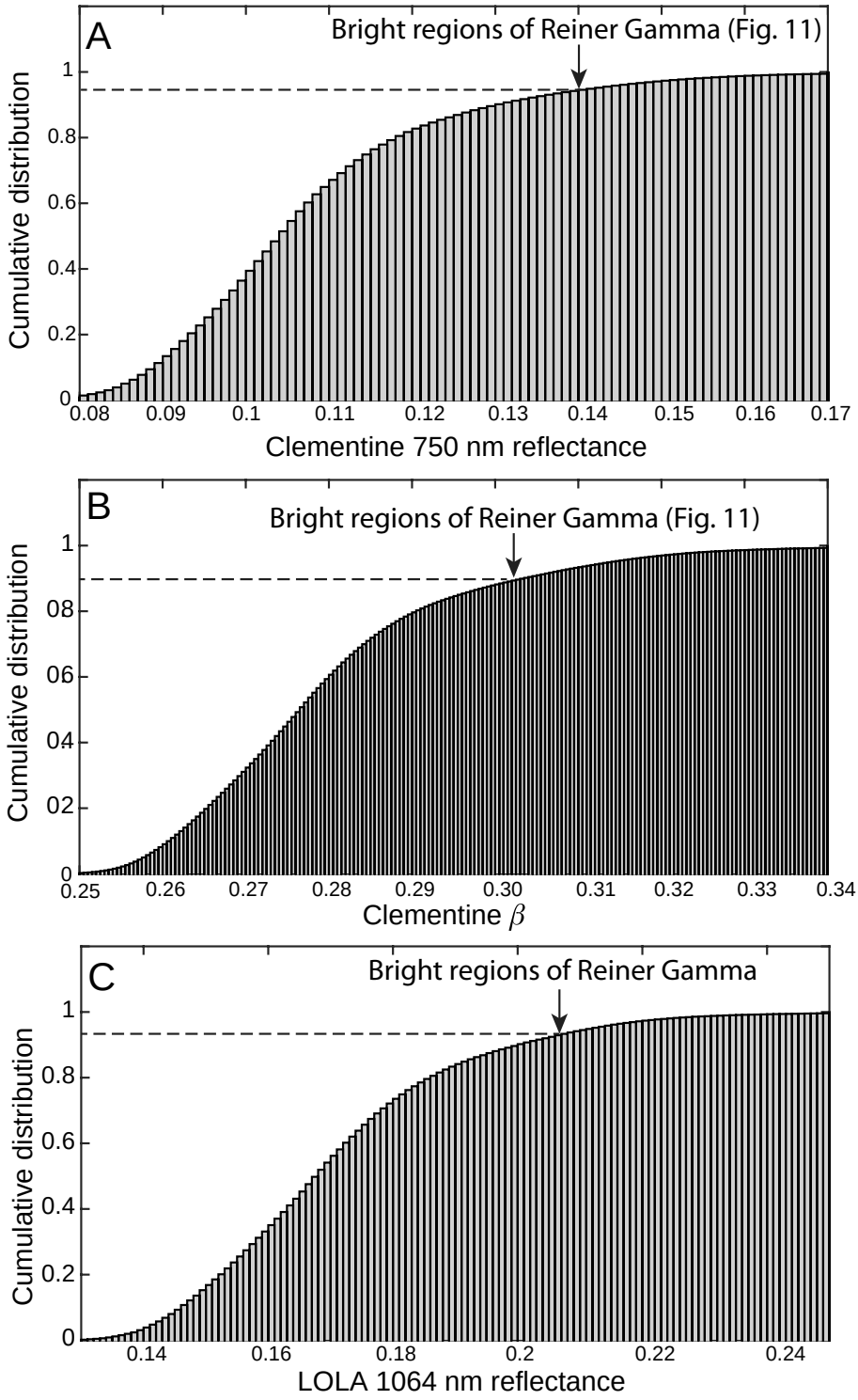

Fig. 12. Reflectance data from the entire lunar maria. (A) Cumulative distribution of Clementine 750-nm-reflectance. (B) Cumulative distribution of the spectral parameter β. (C) Cumulative distribution of LOLA 1064 nm reflectance. The peak non-crater value obtained from the regions in black boxes in Fig. 11 is shown for comparison. The map of LOLA reflectance is not shown in Fig. 11 due to its low resolution (4 ppd).

observed (i.e. between 0° and ± 65° N, Fig. 9). This finding is broadly consistent with Trang and Lucey (2019) who found that submicroscopic iron abundances saturate in high iron soil, but it is difficult to directly compare their results with ours, as their saturation effect is a summation across all latitudes and terrains. In addition, their iron abundance is derived from MI data (Lemelin et al., 2015), while ours is from the Lunar Prospector GRS.

We suggest that a process operates to prevent sufficient accumulation of submicroscopic iron in low-iron grains, while high iron soils approach saturation. As discussed in Section 1, under this interpretation, grains of any iron content would eventually saturate with submicroscopic iron if left exposed for long enough periods of time. Low

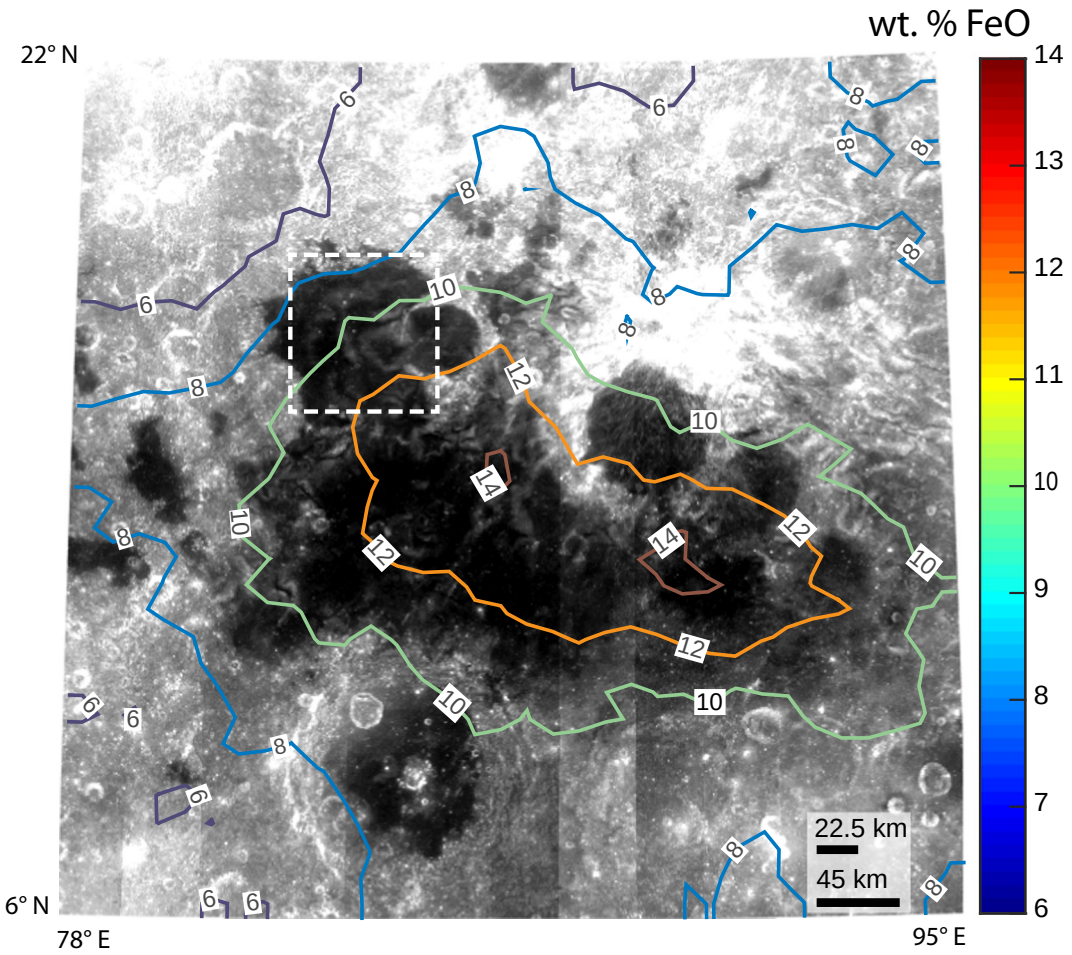

Fig. 13. Lunar Prospector iron contours (wt% FeO) over Clementine 750 nm reflectance at Mare Marginis. The dashed white box indicates the area discussed in the text and shown in Fig. 14. Stereographic projection centered at (18° N, 86° E).

iron grains have less available iron, and therefore reach this saturation state more slowly. At high latitudes, low iron grains reach this state even more slowly, due to the lower solar wind flux. The process competing against accumulation of submicroscopic iron on all such grains is likely the continual destruction and creation of grains through micrometeoroid bombardment, or regolith gardening. This interpretation suggests the timescales of the solar-wind-induced nanophase iron saturation and gardening must therefore be roughly similar. For example, if the nanophase iron saturation timescale were much longer, then there would be no observations of such saturation on the Moon, which we have reported. At the moment, given our lack of understanding of the mechanisms behind production of submicroscopic iron, estimating the actual timescales will be difficult. Laboratory particle irradiation experiments suggest 10^5 years of exposure to the solar wind would be required to saturate a grain's optical changes Hapke (2001). In contrast, the time to produce vapor deposited rims or amorphize lunar soil grains is ~10^6–10^7 years (Keller and Zhang, 2015). Much work remains to link the various processes operating over these timescales.

This model for saturation of high iron soils also works if submicroscopic iron is not produced by the solar wind. As discussed in the introduction, there is only limited work demonstrating the exact chemical or physical change (e.g. nanophase or microphase iron production) that arises from ion irradiation and which produces the classic darkening of silicate soils in space. It is possible that grain rim amorphization is the dominant effect of ion irradiation (Christoffersen et al., 2015). Such changes, either on their own, or in combination with micrometeoroid bombardment, may exhibit grain darkening as a function of exposure time. In other words, whatever the exact nature of the grain rim changes taking place with exposure to the solar wind, our suggestion remains that its saturation timescale may compete with gardening and rejuvenation of the soil.

An interesting implication of the above model is that the solar wind flux appears to be fortuitously nearly saturating at the equator for all iron bins. This can be seen by the nearly equal reflectances of equatorial pixels across all iron bins (Fig. 9). This implies that the equatorial rates of soil destruction and refreshing are slow enough relative to the equatorial submicroscopic iron production rate, to permit near-saturation of these soils at any iron bin.

Finally, we highlight yet another complication of our model and space weathering in general: micrometeoroids likely produce submicroscopic iron, but they are also the same agent that refreshes the soil. If micrometeoroid flux substantially decreases with latitude, then its importance in producing spectral changes at high latitudes is not only reduced, but its ability to refresh those soils is similarly reduced. How these effects may balance at varying latitudes is clearly uncertain.

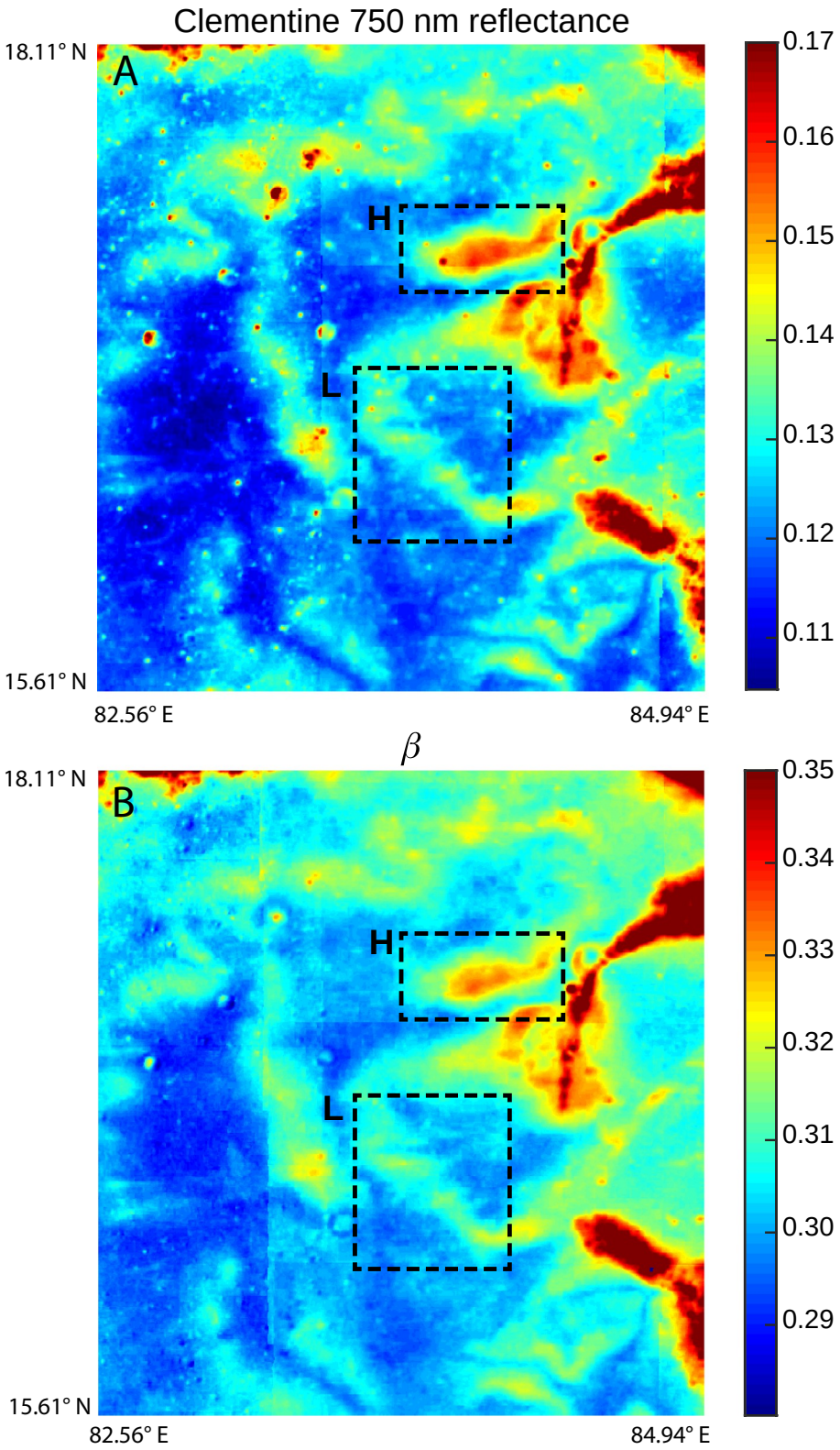

Fig. 14. (A) 750-nm-Clementine reflectance at northwest Mare Marginis (Fig. 13). (B) Spectral parameter β (Clementine derived) at northwest Mare Marginis. Black dashed boxes illustrate the mare swirls discussed in the text. Both maps are cylindrical projection. Both maps are saturated at the high end of the values shown due to the presence of bright highlands material. This saturation does not affect the spectral range occupied by swirl portions of the map.

4.4. Extrapolation to Vesta

We can also predict the effect of solar wind weathering on Vesta's surface. Vesta does not exhibit the same darkening and reddening attributed to lunar-style space weathering (LSSW) (Blewett et al., 2016; Pieters et al., 2012). In contrast, regolith churning and mixing of exogenous materials appear to control the spectra of the surface (Denevi et al., 2016). However, nanophase iron does appear in at least one howardite regolith breccia (Noble et al., 2011), albeit at smaller abundances than in lunar soils. Furthermore, LSSW appears to be important for other asteroids (Vernazza et al., 2009). One hypothesis for this discrepancy is that Vesta has a crustal magnetic field to stand off the solar wind (Fu et al., 2012a; Vernazza et al., 2006), just as at lunar swirls. Our results allow us to predict the amount of spectral change for a Vesta surface of a given iron content in the absence of a magnetic field, at Vesta's semi-major axis of 2.36 AU.

The surface of Vesta is composed mostly of material similar in composition to howardite and eucritic meteorites (McSween et al., 2014), which have typical FeO concentrations of ~17–19 wt% (Warren et al., 2009). Assuming the solar wind flux decreases like the square of the solar distance, Vesta's equator experiences a factor of $(1/2.36^2) = 0.18$ reduction compared to the lunar equator. This flux is equivalent to the flux received at a latitude of 80° N on the Moon, which is outside our analysis range for all of our iron bins. However, setting this limitation aside, and proceeding assuming that the lunar GRS 18–19 wt% FeO bin is sufficiently calibrated to permit direct comparison to the howardite and eucrite FeO content, we can calculate the spectral change at Vesta relative to the same material at the lunar equator. We obtain $\Delta R_{750} = 0.05$ for 80° N. This value is similar to the ~0.06 change from an extrapolation of results in Fig. 4 of Sim et al. (2017). Sim et al. (2017) studied the solar wind's effect on space weathering by examining the spectra of crater walls, as a function of their orbit-averaged exposure to the magnetotail (where solar wind fluxes are reduced). However, their study used data across all iron bins, so it is not possible to make a direct comparison between our prediction and their results. We also ignored the differences in micrometeoroid speeds at lunar and Vesta semi-major axes; the slower values at the latter may increase the expected change in reflectance. Ultimately, further studies of pristine and weathered reflectances of lunar and Vesta-like materials can be compared with these predictions to help predict the magnitude of solar wind weathering at Vesta (if any), and to what degree its surface might be shielded by a magnetic field.

5. Conclusions

We have found that iron content influences a soil's spectral response to changes in weathering fluxes at high latitudes. High iron soils (> 21 wt% gamma-ray FeO) only vary in R_{750} by ~0.01 for flux reductions of ~50%, while low iron soils (14 wt% gamma-ray FeO) experience a five-fold larger change of ~0.05. This is consistent with the idea that accumulation and potential saturation of a soil grain with submicroscopic iron, or some other optically active physical and chemical changes on the rim, is moderated by continual destruction and creation of new grains. Our proposed interpretation is that high iron grains saturate quickly, before they can be destroyed.

Our conclusions are limited by the latitudinal coverage of maria surfaces of diverse iron content. In particular, the highest iron bin we utilized only reaches ± 45° latitude from the equator. We also postulate that non-linear brightening may take place at very low weathering fluxes. Either of these effects could help explain the anomalous ~80% brightness we find at Reiner Gamma, which contains the top 5% brightest pixels on the entire maria. Ultimately, however, in situ or near-surface measurements of solar wind flux at lunar swirls of different iron compositions (e.g. Reiner Gamma and Mare Marginis) would offer a definitive quantification of how the solar wind affects spectral properties of airless silicate bodies.

Acknowledgements

This work was supported by the BK21 plus program through the National Research Foundation (NRF), funded by the Ministry of Education of Korea. CKS acknowledges the support from Basic Science Research Program through the National Research Foundation of Korea (NRF) funded by the Ministry of Education (2016R1A6A3A11931484). SSK was supported by the NRF funded by the Ministry of Science and ICT (2019R1A2C1009004).

Appendix A. Derivation of β from Kaguya data

The spectral parameter β was derived using MAP-level, 2048-ppd mosaics of Kaguya Multiband Imager (MI), downloaded from Kaguya archive (http://darts.isas.jaxa.jp/planet/pdap/selene/). Geometric distortions caused by the topography had been corrected by MI team making use of the parallax between adjacent observational bands of the instrument. Hemingway et al. (2015) defined the spectral parameters α and β as

$$\alpha = R_{750} - \left(\frac{R_{950}}{R_{750}}\right)/m_1$$

$$\beta = R_{750} - \left(\frac{R_{950}}{R_{750}}\right)/m_2$$

where R_{750} and R_{950} are 750 nm and 950 nm reflectances, respectively, and m_1 and m_2 are the slopes of the swirl and impact-related trends, respectively. In Figs. A1–A3, the value of m_2 is the slope of the designated background area for three swirls (marked by red). The value of m_1 is found from the best-fit line through the medians of each spectral region shown. Averaging over the three swirl areas yields m_1 = -2.5 ± 0.3 and $m_2 = -7.3 \pm 0.4$. These values are lower than those found in Hemingway et al. (2015) using Clementine data: $m_1 = -1.6 \pm 0.2$ and $m_2 = -5.7 \pm 0.5$. We ascribe most of the discrepancy to the differences between the reflectances of Clementine/UVVIS and Kaguya/MI (Ohtake et al., 2010).

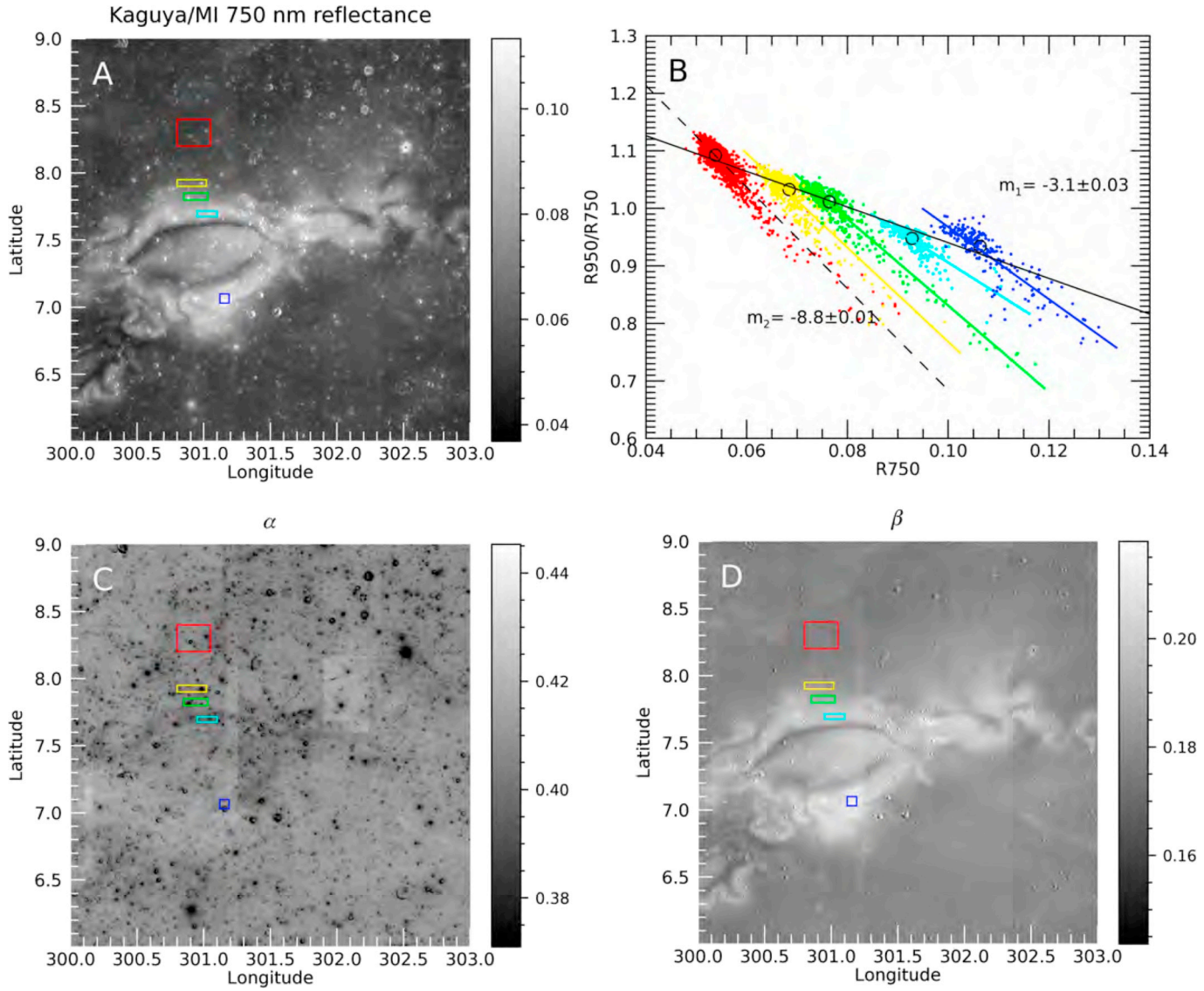

Fig. A1. (A) Kaguya/MI reflectance map of Reiner Gamma swirl at 750 nm. The five colored boxes of interest are the same as those in Fig. 1 of Hemingway et al. (2015). (B) 750 nm reflectance and 950 nm/750 nm band ratio of pixels sampled from the boxes of corresponding colors in (A). Only 1% of the pixels inside each box are shown for clarity. The dashed black line is a linear regression fit of the red point group and has a slope of m_2. The black circles represent the median of each group. The solid black line is a linear fit through the medians and has a slope of m_1. (C) Map of spectral parameter α (refer to Hemingway et al., 2015 for detailed description). (D) Map of β parameter.

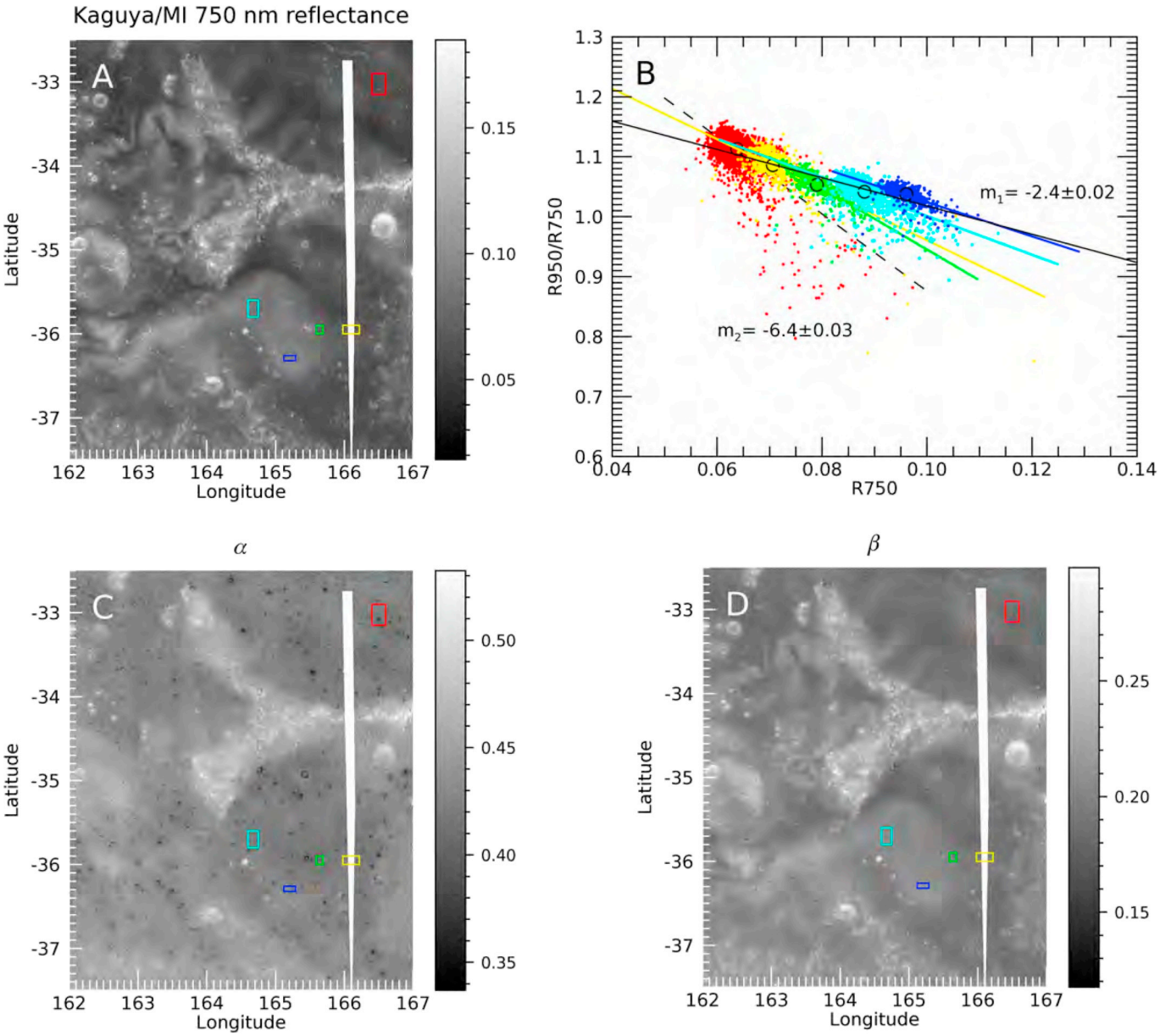

Fig. A2. Same as Fig. A1 but for Mare Ingenii swirls.

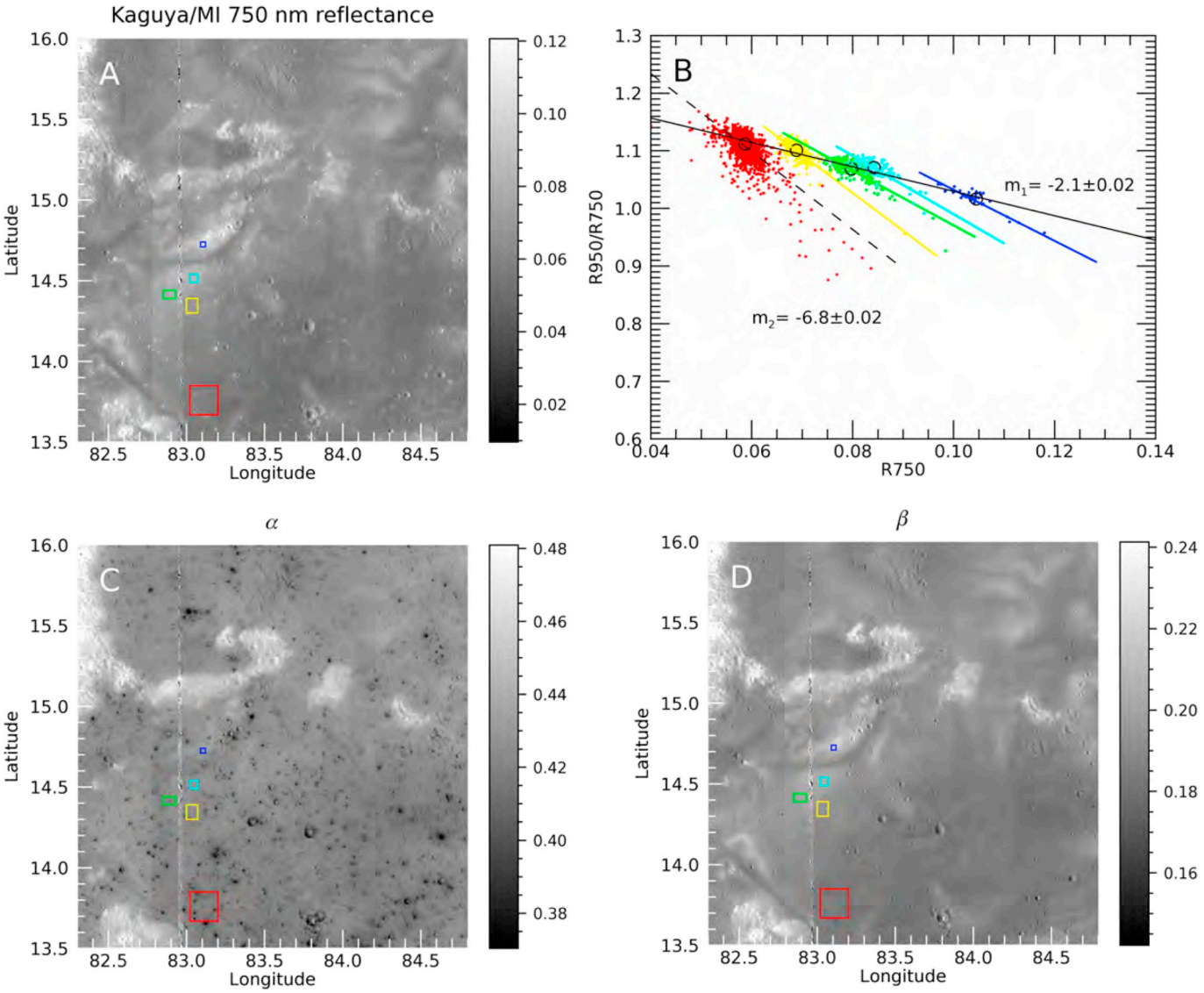

Fig. A3. Same as Fig. A1 but for Mare Marginis swirls.

References

Blewett, D.T., et al., 2016. Optical space weathering on Vesta: radiative-transfer models and Dawn observations. Icarus 265, 161–174.

Britt, D.T., Pieters, C.M., 1994. Darkening in black and gas-rich ordinary chondrites: the spectral effects of opaque morphology and distribution. Geochim. Cosmochim. Acta 58, 3905–3919.

Christoffersen, R., Dukes, C.A., Keller, L.P., Rahman, Z., Baragiola, R.A., 2015. Problems at the leading edge of space weathering as revealed by TEM combined with surface science techniques. In: Space Weathering of Airless Bodies: An Integration of Remote Sensing Data, Laboratory Experiments and Sample Analysis Workshop, pp. 2065 edited.

Denevi, B.W., et al., 2016. Global variations in regolith properties on asteroid Vesta from Dawn's low-altitude mapping orbit. Meteorit. Planet. Sci. 51, 2366–2386.

Domingue, D.L., et al., 2014. Mercury's weather-beaten surface: understanding mercury in the context of lunar and asteroidal space weathering studies. Space Sci. Rev. 181, 121–214.

Fu, R.R., Weiss, B.P., Shuster, D.L., Gattacceca, J., Grove, T.L., Suavet, C., Lima, E.A., Li, L., Kuan, A.T., 2012a. An ancient Core dynamo in asteroid Vesta. Science 338, 238.

Fu, X., Zou, Y., Zheng, Y., Ouyang, Z., 2012b. Effects of space weathering on diagnostic spectral features: results from He+ irradiation experiments. Icarus 219, 630–640.

Gallant, J., Gladman, B., Ćuk, M., 2009. Current bombardment of the earth-moon system: emphasis on cratering asymmetries. Icarus 202, 371–382.

Garrick-Bethell, I., Head, J.W., Pieters, C.M., 2011. Spectral properties, magnetic fields, and dust transport at lunar swirls. Icarus 212 (2), 480–492. https://doi.org/10.1016/j.icarus.2010.11.036.

Gault, D. E., F. Hoerz, D. E. Brownlee, and J. B. Hartung (1974), Mixing of the lunar regolith, in Lunar and Planetary Science Conference Proceedings, edited, pp. 2365–2386.

Hapke, B., 2001. Space weathering from mercury to the asteroid belt. J. Geophys. Res. 106, 10039–10074.

Hemingway, D.J., Garrick-Bethell, I., Kreslavsky, M.A., 2015. Latitudinal variation in spectral properties of the lunar maria and implications for space weathering. Icarus 261, 66–79.

Hood, L.L., Schubert, G., 1980. Lunar magnetic anomalies and surface optical properties. Science 208, 49–51.

James, C.L., Basu, A., Wentworth, S.J., McKay, D.S., 2001. Grain size distribution of Fe0 globules in lunar agglutinitic glass: First results from Apollo 17 soil 78421. In: GSA Ann. Meet, (Abstract #27433).

Jeong, M., Kim, S.S., Garrick-Bethell, I., Park, S.-M., Sim, C.K., Jin, H., Min, K.W., Choi, Y.-J., 2015. Multi-band polarimetry of the lunar surface. I. Global properties. Astrophys. J. Suppl. Ser. 221.

Keller, L. P., and S. Zhang (2015), Rates of space weathering in lunar soils, in Space Weathering of Airless Bodies: An Integration of Remote Sensing Data, Laboratory Experiments and Sample Analysis Workshop, edited, p. 2056.

Kohout, T., et al., 2014. Space weathering simulations through controlled growth of iron nanoparticles on olivine. Icarus 237, 75–83.

Kreslavsky, M.A., Head, J.W., Neumann, G.A., Rosenburg, M.A., Aharonson, O., Smith, D.E., Zuber, M.T., 2013. Lunar topographic roughness maps from Lunar Orbiter Laser Altimeter (LOLA) data: scale dependence and correlation with geologic features and units. Icarus 226, 52–66.

Lawrence, D.J., Feldman, W.C., Elphic, R.C., Little, R.C., Prettyman, T.H., Maurice, S., Lucey, P.G., Binder, A.B., 2002. Iron abundances on the lunar surface as measured by the Lunar Prospector gamma-ray and neutron spectrometers. Journal of Geophysical Research (Planets) 107, 5130.

Le Feuvre, M., Wieczorek, M.A., 2008. Nonuniform cratering of the terrestrial planets. Icarus 197, 291–306.
Lemelin, M., Lucey, P.G., Neumann, G.A., Mazarico, E.M., Barker, M.K., Kakazu, A., Trang, D., Smith, D.E., Zuber, M.T., 2016. Improved calibration of reflectance data from the LRO Lunar Orbiter Laser Altimeter (LOLA) and implications for space weathering. Icarus 273, 315–328.
Lemelin, M., Lucey, P.G., Song, E., Taylor, G.J., 2015. Lunar central peak mineralogy and iron content using the Kaguya Multiband Imager: reassessment of the compositional structure of the lunar crust. Journal of Geophysical Research (Planets) 120, 869–887.
Loeffler, M.J., Baragiola, R.A., Murayama, M., 2008. Laboratory simulations of re-deposition of impact ejecta on mineral surfaces. Icarus 196, 285–292.
Loeffler, M.J., Dukes, C.A., Baragiola, R.A., 2009. Irradiation of olivine by 4 keV He+: simulation of space weathering by the solar wind. Journal of Geophysical Research (Planets) 114, 3003.
Lucey, P.G., Blewett, D.T., Jolliff, B.L., 2000a. Lunar iron and titanium abundance algorithms based on final processing of Clementine ultraviolet-visible images. J. Geophys. Res. 105, 20297–20306.
Lucey, P.G., Blewett, D.T., Taylor, G.J., Hawke, B.R., 2000b. Imaging of lunar surface maturity. J. Geophys. Res. 105, 20377–20386.
Lucey, P.G., Riner, M.A., 2011. The optical effects of small iron particles that darken but do not redden: evidence of intense space weathering on Mercury. Icarus 212, 451–462.
Lucey, P.G., Taylor, G.J., Malaret, E., 1995. Abundance and distribution of iron on the moon. Science 268, 1150–1153.
Lucey, P.G., et al., 2014. The global albedo of the moon at 1064 nm from LOLA. Journal of Geophysical Research (Planets) 119, 1665–1679.
Marchi, S., Brunetto, R., Magrin, S., Lazzarin, M., Gandolfi, D., 2005. Space weathering of near-Earth and main belt silicate-rich asteroids: observations and ion irradiation experiments. Astron. Astrophys. 443, 769–775.
McSween, H.Y., De Sanctis, M.C., Prettyman, T.H., 2014. Unique, Antique Vesta. Elements 10, 39–44.
Nesvorný, D., Jedicke, R., Whiteley, R.J., Ivezić, Ž., 2005. Evidence for asteroid space weathering from the Sloan Digital Sky Survey. Icarus 173, 132–152.
Noble, S.K., Keller, L.P., Pieters, C.M., 2011. Evidence of space weathering in regolith breccias II: Asteroidal regolith breccias. Meteorit. Planet. Sci. 45, 2007–2015.
Ohtake, M., Haruyama, J., Matsunaga, T., Yokota, Y., Morota, T., Honda, C., 2008. Performance and scientific objectives of the SELENE (KAGUYA) Multiband Imager. Earth, Planets, and Space 60, 257–264.
Ohtake, M., et al., 2010. Deriving the absolute reflectance of lunar surface using SELENE (Kaguya) multiband imager data. Space Sci. Rev. 154, 57–77.
Pieters, C.M., Noble, S.K., 2016. Space weathering on airless bodies. Journal of Geophysical Research (Planets) 121, 1865–1884.
Pieters, C.M., et al., 2012. Distinctive space weathering on Vesta from regolith mixing processes. Nature 491, 79–82.
Prettyman, T.H., Hagerty, J.J., Elphic, R.C., Feldman, W.C., Lawrence, D.J., McKinney, G.W., Vaniman, D.T., 2006. Elemental composition of the lunar surface: analysis of gamma ray spectroscopy data from lunar prospector. Journal of Geophysical Research (Planets) 111.
Sasaki, S., Hiroi, T., Nakamura, K., Hamabe, Y., Kurahashi, E., Yamada, M., 2002. Simulation of space weathering by nanosecond pulse laser heating: dependence on mineral composition, weathering trend of asteroids and discovery of nanophase iron particles. Adv. Space Res. 29, 783–788.
Sato, H., Robinson, M.S., Lawrence, S.J., Denevi, B.W., Hapke, B., Jolliff, B.L., Hiesinger, H., 2017. Lunar mare TiO2 abundances estimated from UV/Vis reflectance. Icarus 296, 216–238.
Sim, C.K., Kim, S.S., Lucey, P.G., Garrick-Bethell, I., Choi, Y.-J., 2017. Asymmetric space weathering on lunar crater walls. Geophys. Res. Lett. 44, 11.
Strazzulla, G., Dotto, E., Binzel, R., Brunetto, R., Barucci, M.A., Blanco, A., Orofino, V., 2005. Spectral alteration of the meteorite Epinal (H5) induced by heavy ion irradiation: a simulation of space weathering effects on near-Earth asteroids. Icarus 174, 31–35.
Trang, D., Lucey, P.G., 2019. Improved space weathering maps of the lunar surface through radiative transfer modeling of Kaguya multiband imager data. Icarus 321, 307–323.
Trang, D., Lucey, P.G., Izenberg, N.R., 2017. Radiative transfer modeling of MESSENGER VIRS spectra: detection and mapping of submicroscopic iron and carbon. Icarus 293, 206–217.
Vernazza, P., Binzel, R.P., Rossi, A., Fulchignoni, M., Birlan, M., 2009. Solar wind as the origin of rapid reddening of asteroid surfaces. Nature 458, 993–995.
Vernazza, P., Brunetto, R., Strazzulla, G., Fulchignoni, M., Rochette, P., Meyer-Vernet, N., Zouganelis, I., 2006. Asteroid colors: a novel tool for magnetic field detection? The case of Vesta. Astron. Astrophys. 451, L43–L46.
Warren, P.H., Kallemeyn, G.W., Huber, H., Ulff-Moller, F., Choe, W., 2009. Siderophile and other geochemical constraints on mixing relationships among HED-meteoritic breccias. Geochim. Cosmochim. Acta 73, 5918–5943.
Wilcox, B.B., Lucey, P.G., Gillis, J.J., 2005. Mapping iron in the lunar mare: an improved approach. Journal of Geophysical Research (Planets) 110.
Yokota, Y., et al., 2011. Lunar photometric properties at wavelengths 0.5-1.6 μm acquired by SELENE spectral profiler and their dependency on local albedo and latitudinal zones. Icarus 215, 639–660.